Draft version May 21, 2022
Typeset using LaTeX default style in AASTeX63

A new mode of geodynamics in the Hadean facilitates the emergence of early life

Yoshinori Miyazaki[1,2] and Jun Korenaga[1]

[1] *Department of Earth and Planetary Sciences, Yale University*
New Haven, CT 06511, USA
[2] *Division of Geological and Planetary Sciences, California Institute of Technology*
Pasadena, CA 91125, USA

(Received August 3, 2020; Revised April 10, 2021; Accepted December 20, 2021)

Submitted to Nature

ABSTRACT

The Hadean eon, following the global-scale melting of the mantle(Matsui & Abe 1986; Tonks & Melosh 1993; Canup & Asphaug 2001), is expected to be a dynamic period, during which Earth experienced vastly different conditions. Geologic records, however, suggest that the surface environment of Earth was already similar to the present by the middle of the Hadean(Wilde et al. 2001; Harrison 2009). Under what conditions a fiendish surface environment could turn into a habitable one remains uncertain(Sleep & Zahnle 2001). Here we show that a hydrated mantle with small-scale chemical heterogeneity, created as a result of magma ocean solidification, is the key to ocean formation, the onset of plate tectonics, and the rapid removal of greenhouse gases, which are all essential to create a habitable environment on terrestrial planets. When the mantle is wet and dominated by high-magnesium pyroxenites, the removal of carbon dioxide from the atmosphere is expected to be >10 times faster than the case of a pyrolitic homogeneous mantle and could be completed within ∼160 Myr. Such a chemically heterogeneous mantle would also produce oceanic crust rich in olivine, which is reactive with ocean water and promote serpentinization. Therefore, conditions similar to the Lost City Hydrothermal Field(Kelley et al. 2005; Proskurowski et al. 2008; Klein et al. 2019) may have existed globally in the Hadean seafloor.

The Hadean Earth is often viewed as an uninhabitable world with a partially molten surface, active volcanism, and a hot steamy atmosphere. The picture of harsh surface conditions may be expected from the Moon-forming giant impact(Matsui & Abe 1986; Tonks & Melosh 1993) and the subsequent bombardment by leftover planetesimals(Raymond et al. 2013), but ancient geological records suggest that by ∼4.3 Ga, the Earth's surface has become similar to the present-day environment with oceans and granitic crust(Wilde et al. 2001; Harrison 2009). Hadean detrital zircons, enriched in heavy oxygen and yielding low melting temperatures, indicate that liquid water was already present at the Earth's surface. Furthermore, by the end of the Hadean, the global carbon cycle had likely stabilized the climate and maintained a surface temperature similar to the present day(Krissansen-Totton et al. 2018). The first 500 Myr of our planet, therefore, should have experienced a dramatic change in the climate, evolving quickly from being uninhabitable to habitable.

The troposphere during the early Hadean is believed to comprise greenhouse gases released during the solidification of a magma ocean(Elkins-Tanton 2008; Lebrun et al. 2013; Hamano et al. 2013; Salvador et al. 2017; Bower et al. 2019). The composition and redox state of the early atmosphere have been a subject of discussion(Hirschmann 2012; Deng et al. 2020), but Earth likely had a thick atmosphere of CO_2 and H_2O, which maintained an extreme climate on the early Earth(Abe 1993a; Lebrun et al. 2013). To create a habitable environment within the Hadean period, most of greenhouse gases must be removed from the atmosphere within the same timescale. Indeed, the atmospheric pressure of CO_2 is estimated to have been lower than 1 bar at the end of the Hadean(Krissansen-Totton et al. 2018; Catling & Zahnle 2020). CO_2, the major constituent of greenhouse gases, can be sequestered into the Earth's interior by being transformed into carbonate minerals at ocean basins, and then subducted to the mantle(Sleep & Zahnle 2001). It remains unclear, however, whether the sequestration was efficient enough to produce a habitable environment by

~4.0 Ga. In this study, this question is addressed by delineating the mode of geodynamics during the Hadean. We first investigate the efficiency of mantle degassing during the solidification of a magma ocean, which is crucial for constraining the degree of hydration and thus the rheology of the Hadean mantle. We then turn to quantify the surface renewal rate and examine the rate of carbon sequestration.

INEFFICIENT DEGASSING OF A MAGMA OCEAN

First of all, an efficient degassing of the mantle is unlikely during the solidification of a magma ocean if a rheological transition in a partially molten medium is taken into account. A magma ocean behaves rheologically as solid when melt fraction becomes lower than a certain threshold (a typical value assumed in magma ocean studies is 40%(Abe 1993a; Solomatov 2007)), and if percolation is not rapid enough, volatiles would be trapped in the porous melt phase(Hier-Majumder & Hirschmann 2017). Volatiles, in particular water, would remain dissolved in the melt phase until melt fraction becomes lower than 0.2 wt%. Melt can contain water by more than 50 wt% at high pressures(Kawamoto & Holloway 1997; Katz et al. 2003) and that the initial water mantle inventory is estimated to be 0.04–0.1 wt%(Hirschmann & Dasgupta 2009; Korenaga et al. 2017). Furthermore, the newly formed solid matrix would be continuously transported downwards by the Rayleigh-Taylor instability(Maurice et al. 2017; Miyazaki & Korenaga 2019), and because the downwelling velocity of the instability is faster than melt percolation(Solomatov 2007), volatiles would be sequestered in the deep mantle. Therefore, water would either be trapped in the solid matrix as bubbles or would diffuse into the surrounding nominally anhydrous minerals. This indicates that a large fraction of water would remain in the mantle even after the solidification (Figure 1). If volatiles, behaving as incompatible elements, concentrates at the surface melt layer as magma ocean solidifies from the bottom to the top(Elkins-Tanton 2008; Lebrun et al. 2013; Hamano et al. 2013), volatile concentrations eventually exceed saturation levels, but such a high concentration of volatiles would not be reached if the rheological transition is taken into account.

The mass of atmosphere degassed from a magma ocean, therefore, is likely to be smaller than predicted in refs. (Elkins-Tanton 2008; Lebrun et al. 2013; Hamano et al. 2013; Salvador et al. 2017; Bower et al. 2019). With this effect of rheological transition on degassing(Hier-Majumder & Hirschmann 2017), we predict the evolution of atmospheric mass during magma ocean solidification using volatile partitioning between the atmosphere and the surface of a magma ocean. Because the solubilities of volatiles increase with pressure, those at the surface govern the volatile budget of the mantle. Figure 2a illustrates that while ~80% of the total carbon inventory would reside in the atmosphere, ~99% of water would remain in the mantle. Here we assume that the mantle contained between 0.04 and 0.1 wt% of H_2O (corresponding to ~1.2 and 3 ocean mass, respectively) and 200–500 ppm of CO_2, based on estimates for the present-day volatiles budget(Hirschmann & Dasgupta 2009; Korenaga et al. 2017). We find that the atmospheric pressure of volatiles is mostly constant during the evolution because, when volatiles are trapped in the porous melt phase, the solidification process has a negligible effect on volatile concentration in the magma ocean. The atmospheric pressure increases by a small degree during the final stage of solidification as surface magma starts to solidify and volatiles become enriched in the melt phase (Figure 2a). Even so, with an initial water inventory is ~1.2 ocean, the surface water is limited to ~0.011 ocean mass with a partial pressure of ~7 bar (Figure 2a). On the other hand, a large fraction of CO_2 would be degassed to the atmosphere from the beginning of the evolution because CO_2 is less soluble than H_2O in silicate melt(Blank & Brooker 1994; Hier-Majumder & Hirschmann 2017). Our partitioning model predicts that the partial pressure of CO_2 would be ~110 and 290 bar with initial concentrations of 200 and 500 ppm, respectively.

Surface water is likely supplemented by another degassing after the disappearance of the melt-dominated layer. When the surface of a magma ocean behaves rheologically as melt (Figure 1a), high convective heat flux, supported by low melt viscosity, maintains a high surface temperature above 1000 °C (Figure 2b)(Lebrun et al. 2013; Salvador et al. 2017). When cooling proceeds and the surface becomes rheologically solid (Figure 1b), however, convective heat flux decreases by orders of magnitude, and a 1-D atmospheric model suggests the surface temperature drops discontinuously to a temperature below the mantle solidus. At this point, the Rayleigh-Taylor instability, which can happen rapidly and frequently(Miyazaki & Korenaga 2019), should have cooled the mantle, changing the mantle thermal structure to be adiabatic from superadiabatic, and solid-sate convection would govern the cooling thereafter(Abe 1993b; Solomatov 2007). Timescale comparison suggests that solid-state convection is slower than upward melt percolation in the upper mantle (see Methods), so residual melt in the shallow upper mantle would percolate upward and erupt to the surface. Based on a mantle melting model, we predict that the top ~4 GPa of the upper mantle (Figure 1b, Extended Data Figure 1a) was partially molten at the beginning of solid-state convection, and volatiles in this layer

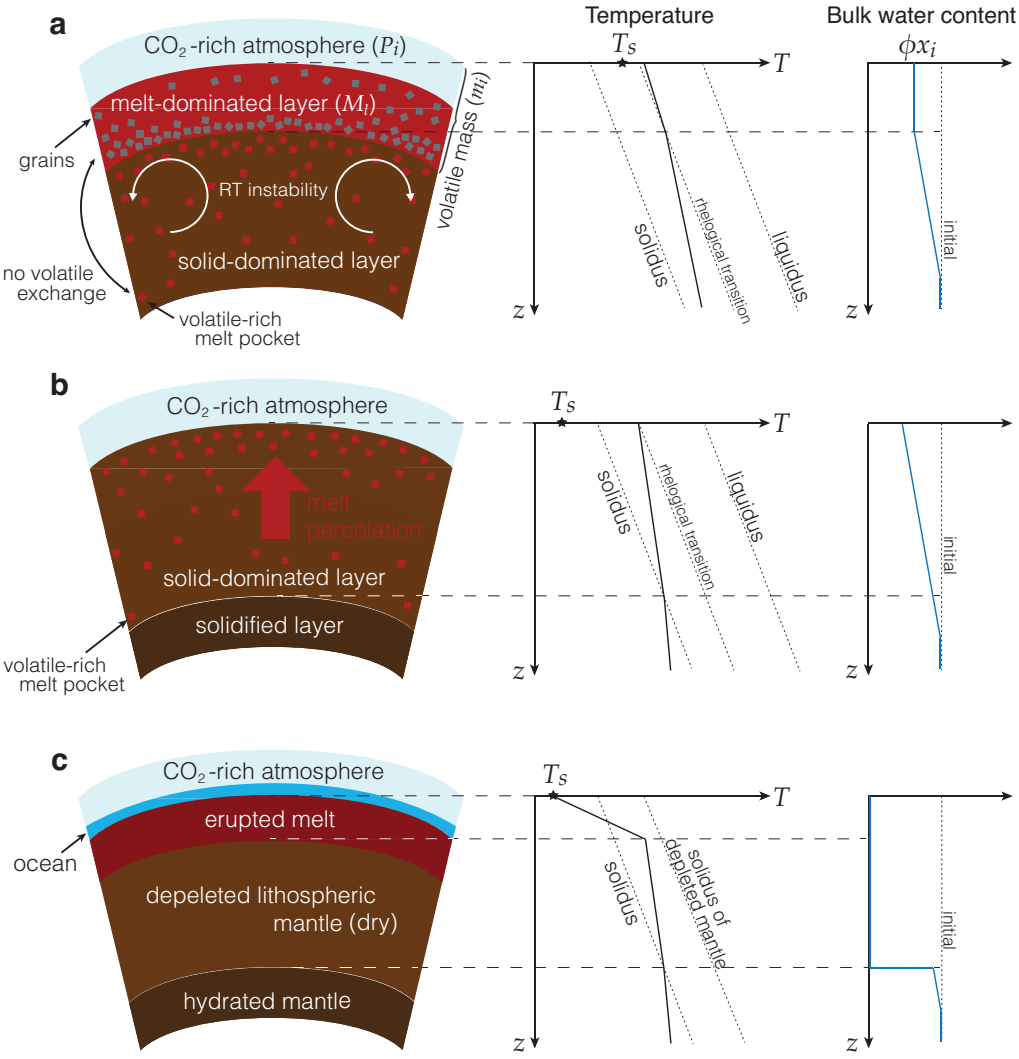

Figure 1. Schematic illustration of how a magma ocean solidifies with the evolution of atmosphere. Only the shallow mantle is illustrated here. **a.** A magma ocean solidifies from the bottom, and the porous melt phase emerges in regions where melt fraction falls below a critical value. Volatiles in the deep mantle are stored in such a residual melt phase instead of being concentrated near the surface. Note that a magma ocean has two rheologically distinct layers, the melt- and solid-dominated. The former is mixed by rapid convection, whereas the latter by the Rayleigh-Taylor instability, both creating an adiabatic thermal profile. Parameters used in Equation (1) (Methods) are labeled to corresponding reservoirs. **b.** When the melt-dominated layer diminishes, convective heat flux plummets, and the surface temperature (star) drops below the mantle solidus. Melt percolation governs the subsequent evolution because solid-state convection is slow. **c.** Erupted melt from the residual melt phase forms a solidified lid, leaving a depleted dry mantle behind. By releasing dissolved volatiles to the atmosphere, the atmosphere contains an enough amount of volatile to form oceans on a cooled surface. The deeper region of the mantle is completely solidified and thus would not degas by percolation. Although it is not shown here, the deeper region contains small-scale iron-rich blobs because we consider a chemically heterogeneous mantle in this study (Figure 3a).

was likely extracted to the atmosphere. For the case of ∼0.04 wt% initial water content, a total of ∼0.06 ocean mass of water is released to the atmosphere, creating ∼36 atm of water vapor atmosphere (Figures 2a, Extended Data Table 1). This exceeds a threshold of ∼0.05 ocean mass to form water oceans when the atmosphere contains ∼200 bar of CO_2(Abe 1993a), so the presence of ocean is plausible immediately after the solidification of a magma ocean. The surface temperature exceeds ∼100 °C due to greenhouse effect, yet liquid water is stabilized by high atmospheric pressure. At the same time, the mantle would still contain a large fraction of water and is expected to be hydrated, lowering the viscosity(Hirth & Kohlstedt 1996; Jain et al. 2019) of the Hadean mantle.

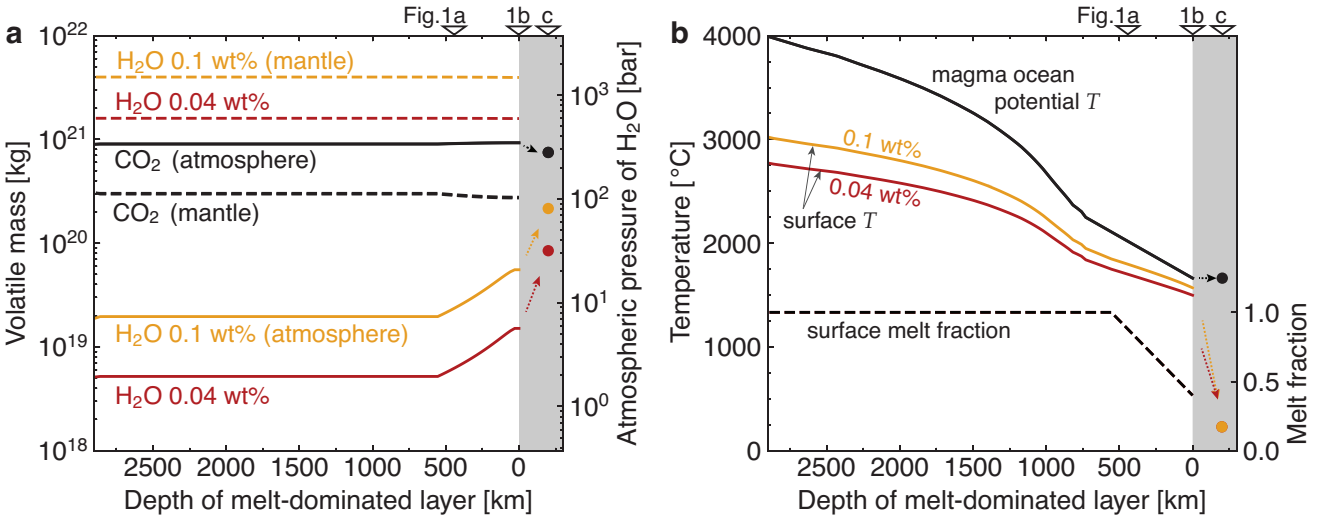

Figure 2. Mantle degassing considering the effect of the rheological transition. Figures are shown as a function of the depth of a melt-dominated layer, and the system evolves from left to right as solidification proceeds. **a.** The volatile budgets of H_2O (colored) and CO_2 (black) in the atmosphere (solid) and the mantle (dashed). **b.** Surface temperature (colored), the potential temperature of magma ocean (black), and the surface melt fraction (dashed). The corresponding atmospheric pressures of H_2O are shown in the right axis. The H_2O contents are coded by color as 0.04 (red) and 0.1 (yellow), corresponding to 1.2 and 3 ocean mass, respectively. Here, the initial CO_2 concentration in the mantle is set to 300 ppm. Dots in shaded regions indicate the state after the complete solidification as described in Figure 1c. For concentrations in the mantle, values after the complete solidification are not shown because only the uppermost layer is affected by melt percolation, and volatiles concentrations in the deeper region remain unchanged.

RAPID PLATE MOTION OF A HYDRATED AND CHEMICALLY HETEROGENEOUS MANTLE

We now turn to the second question of carbon sequestration. With the presence of oceans, the operation of plate tectonics is theoretically possible even in the early Hadean(Korenaga 2011, 2020), so CO_2 could be removed by the formation and subduction of carbonate minerals. The partial pressure of CO_2 is estimated to have been below 1 bar by the end of the Hadean(Krissansen-Totton et al. 2018; Catling & Zahnle 2020), so >100 bar of CO_2 has to be transported back into the mantle. The frequent renewal of the surface by rapid cooling has been proposed as a possible mechanism(Sleep & Zahnle 2001; Zahnle et al. 2007), but contrary to a common belief, a hotter mantle in the past points to more sluggish plate motion because of thicker depleted lithospheric mantle(Korenaga 2003, 2011). Slow plate motion of a hotter mantle, in fact, is corroborated with a range of geological records(Bradley 2008; Herzberg et al. 2010; Pehrsson et al. 2016). Moreover, the Hadean mantle could have been chemically stratified as a result of an overturn after the solidification of magma ocean, with iron-rich dense materials at the bottom(Elkins-Tanton 2008). If so, the mantle would be resistant to thermal convection(Plesa et al. 2014), and plate motion would be even slower, if not totally absent. A hotter mantle in the Hadean, therefore, does not necessarily indicate the rapid sequestration of CO_2.

We propose that rapid recycling is possible with a chemically heterogeneous mantle, which results from the fractional crystallization of a magma ocean(Miyazaki & Korenaga 2019). The differentiation of a magma ocean is driven by the settling and sedimentation of a liquidus mineral, bridgmanite, at the base of the melt-dominated layer. Consequently, high-Mg# (defined as molar Mg/(Mg+Fe)×100) and SiO_2-rich materials would constitute the lower mantle, whereas the upper mantle would be comprised of residual iron-rich dense materials (Figure 3a). Our scaling analysis suggests that such a gravitationally unstable structure is subject to small-scale Rayleigh-Taylor instabilities with a length scale shorter than 100 km(Miyazaki & Korenaga 2019). At the end of solidification, iron-rich materials would thus have existed as small blobs embedded in a high-Mg# pyroxenite matrix (Figure 3a). As explained in detail later, such a mantle with small-scale heterogeneity would not develop thick depleted lithospheric mantle, so rapid plate motion and efficient carbon sequestration could be achieved. In the following, we estimate the surface evolution timescales for both homogeneous and heterogeneous mantles. Our results suggest that the chemically heterogeneous mantle is more compatible with creating a habitable environment by the end of the Hadean.

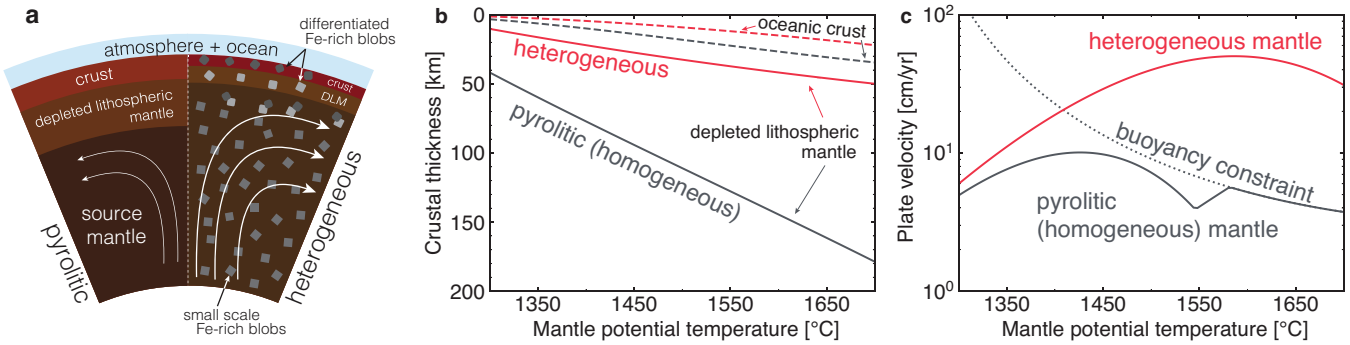

Figure 3. Crustal thickness and plate velocity of chemically heterogeneous and pyrolitic (homogeneous) mantles. **a.** Schematic illustration of the near-surface structure for pyrolitic (left) and chemically heterogeneous (right) mantles. **b.** Estimated thicknesses of oceanic crust (dashed) and depleted lithospheric mantle (solid lines) for different mantle potential temperatures. Color indicates chemically heterogeneous (red) and pyrolitic homogeneous mantles (gray). **c.** Plate velocities for different mantle potential temperatures. A stiff depleted lithospheric mantle is thicker for a pyrolitic homogeneous mantle, resulting in more sluggish plate motion for a hotter mantle. The plate velocity of a mantle hotter than 1590 °C would be further limited by a buoyancy constraint (dotted). With thicker oceanic crust, a longer cooling time or a thicker thermal boundary layer is required for plate to be negatively buoyant. A mantle water content of 0.1 wt% is assumed here.

The chemically heterogeneous mantle is predicted to experience limited dehydration at mid-ocean ridges. Modeling of magma ocean solidification suggests that the pyroxenite matrix has an average Mg# of 94 and constitutes ∼75% of the mantle(Miyazaki & Korenaga 2019). The high-Mg# pyroxenite yields a higher solidus than a homogeneous pyrolitic mantle, and with a mantle potential temperature of 1600 °C, the Rhyolite-MELTS and pMELTS models(Ghiorso et al. 2002; Gualda et al. 2012) predict that the initial depth of melting is ∼4 GPa with 0.1 wt% of water (Extended Data Figure 1a). As the mantle undergoes fractional melting, the pyroxenite matrix becomes mostly dehydrated at ∼2 GPa and forms a depleted lithospheric mantle of 40 km thickness (Extended Data Figure 1b). Iron-rich blobs would also melt during their upwelling, but because they are of small scale, their melting would not contribute to producing a uniformly thick depleted lithospheric mantle. Stress necessary to bend plates is smaller with thinner depleted lithospheric mantle, whereas stress due to the negative buoyancy of plates increases under a higher potential temperature, so the operation of plate tectonics is plausible (see Methods). Pyrolite, on the other hand, starts to melt at a depth deeper than 10 GPa, and because it is rich in olivine, which is less compatible with water than pyroxene, a pyrolitic mantle would dehydrate faster than pyroxenite. Crust and depleted lithospheric mantle are thus estimated to be as thick as ∼26 km and ∼145 km, respectively, at a mantle temperature 250 K hotter than the present (Figure 3b, Extended Data Figure 2).

Thin depleted lithospheric mantle is a key for rapid plate motion under a hotter mantle. Because the depleted lithospheric mantle is drier and thus stiffer, thicker lithosphere results in slower convection than the present-day mantle(Korenaga 2006) (Figure 3c). Also, the presence of thick buoyant crust would require a longer cooling time for plate to be negatively buoyant(Davies 1992), which would further limit the plate velocity. The scaling of plate tectonic convection(Korenaga 2010) suggests that, for a pyroitic mantle, average plate velocity would remain the same as the present at a potential temperature of 1600 °C. In contrast, the depleted lithospheric mantle of chemically heterogeneous mantle is thin enough to allow for rapid plate motion, and its crust is only marginally chemically buoyant because of crust produced from iron-rich blobs, which has a density greater than 3500 kg m^{-3} (Extended Data Table 2) and would help to negate the chemical buoyancy of oceanic crust. Plate velocity for the heterogeneous mantle is estimated to be ∼50 cm yr^{-1} (Figure 3c), and ocean basins would be renewed every ∼9 Myr, allowing the rapid recycling of carbonate minerals. It is noted that, if the mantle had degassed completely during magma ocean solidification, the whole mantle would be dry and stiff, and its viscosity would be ∼50 times higher than that of the present-day mantle, even considering the effect of a higher temperature(Hirth & Kohlstedt 1996; Jain et al. 2019). Plate velocity would be limited to ∼2 cm yr^{-1} (see Methods), and the surface renewal rate becomes smaller than that of a pyrolitic mantle.

Furthermore, the Hadean seafloor could store a greater amount of carbonate minerals because seawater circulating through oceanic crust has a higher CO_2 content. The solubility of CO_2 is higher by at least an order of magnitude under >100 bar than the present-day atmosphere(Diamond & Akinfiev 2003), and thus the alteration of upper oceanic

crust was likely significant. When Ca and Mg in the top 500 m of the crust, a layer with high porosity, were used to form carbonates, an equivalent of ∼22 bar could be stored to the mantle, which is 9 times larger than the present day value of ∼2.5 bar(Alt & Teagle 1999). The P-T path of the Hadean slab would resemble the present-day young subduction zones (Extended Data Figure 3), so some fraction of carbonates may melt and return to the surface. Yet, even assuming that half of subducted carbonates are recycled, 200 bar of CO_2 could be removed from the atmosphere within ∼160 Myr (Figure 4). In contrast, if the mantle were pyrolitic, sluggish plate motion would limit the sequestration of CO_2. Our model predicts that the atmospheric CO_2 remains higher than 10 bar with a surface temperature over 100 °C for ∼1.5 Gyr (Figure 4), which fails to explain the evolution of Earth's atmosphere and surface conditions. If the mantle was pyrolitic in the Hadean, the removal of CO_2 from the atmosphere is unlikely to be completed by the end of Archean.

A high iron-rich olivine content in crust of the chemically heterogeneous mantle (Extended Data Table 2) would promote serpentinization reaction(Sleep et al. 2004), which has an important implication for the earliest life on Earth(Schulte et al. 2006). Serpentinization releases hydrogen and methane by reducing water (Figure 4a), and the anaerobic oxidation of methane is considered to have supported nascent life forms before the beginning of photosynthesis. Methane released by seafloor serpentinization is also observed now at the Lost City hydrothermal vent field (LCHF)(Kelley et al. 2005) located along the Mid-Atlantic Ridge. Microorganisms that use H_2 and CH_4 as chemical energy are known to create diverse biological communities in the LCHF(Proskurowski et al. 2008; Klein et al. 2019), and thus it has been considered as an analog environment to a place where life first appeared on our planet. Given that rocks constituting the LCHF are rich in olivine and have low Si content, a wide exposure of pyroxenite may have created a similar environment to the LCHF at most of the seafloor in the early Hadean. Alkaline conditions may also develop in an environment resembling hydrothermal vents, and combined with the high dissolution rate of olivine, abiotic synthesis of ribose may have occurred(Lambert et al. 2010).

The aftermath of magma ocean solidification has a profound impact on characterizing the surface environment during the Hadean. Given that a habitable environment has emerged by ∼4.0 Gyr ago, the Hadean evolution is explained more naturally by the mantle with a chemically heterogeneous structure. Small-scale heterogeneities would eventually be homogenized with high-Mg# pyroxenite as convective mixing proceeds, but homogenization likely takes a few tens to hundreds million years to complete(Davies 2006). In the meantime, rapid plate motion would have continued. A faster plate motion accompanies a larger flux of upwelling mantle at mid-ocean ridges, so volatiles (including greenhouse gases) in the mantle would efficiently be released to the atmosphere. As sequestration removes CO_2 from the atmosphere, the intake and release of CO_2 would balance after some time, setting an initial condition for the Archean evolution. Also, residual CO_2 may have reacted with hydrogen produced by serpentinization to create a reduced atmosphere (Figure 4). This may explain the potentially high abundance of CH_4 in the Archean atmosphere(Catling & Zahnle 2020). On the other hand, hydrous minerals are vulnerable to dehydration upon subduction, so a rapid plate motion would result in a net increase in surface water through degassing at ridges. Given a higher processing rate than the present-day mantle, the Hadean mantle would have dried out in ∼500 Myr (see Methods), and an initially small ocean mass would have increased to the present-day level or higher by the beginning of the Archean. These are order-of-magnitude arguments but are consistent with the prominent features of the Archean Earth(Korenaga 2011; Korenaga et al. 2017; Catling & Zahnle 2020). Our study provides a new perspective on the evolution of Hadean surface environment by bringing together the models of magma ocean solidification, atmospheric evolution, and mantle convection.

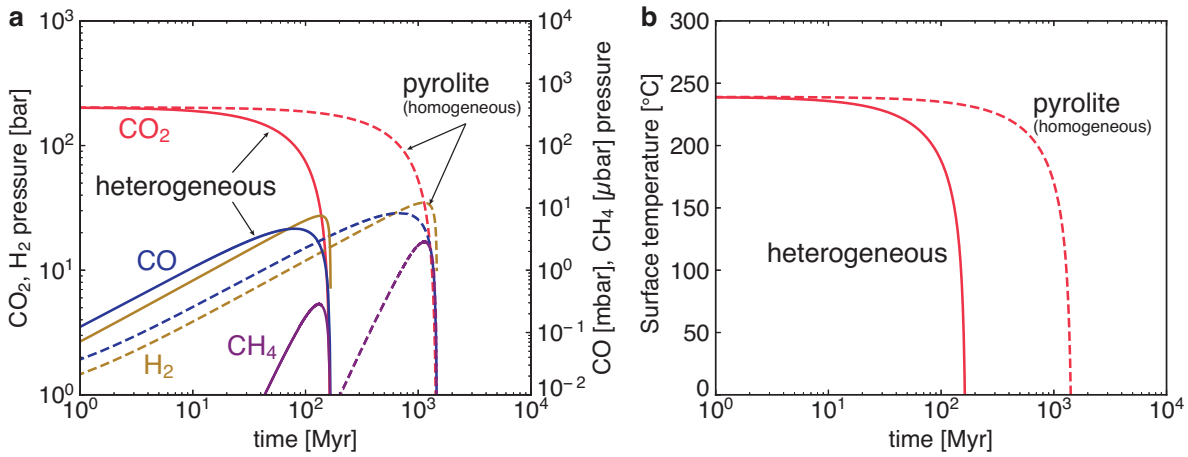

Figure 4. Evolutions of atmospheric composition and surface temperature after the onset of plate tectonics. a. Atmospheric evolution is shown for the cases of chemically heterogeneous (solid) and homogeneous (pyrolitic) mantles (dashed). Color indicates gaseous species: CO_2 (red), CO (blue), H_2 (yellow), and CH_4 (purple). The initial amount of CO_2 is set to 200 bar, which is the amount degassed from a magma ocean with 300 ppm of CO_2, and the model calculations are performed until all CO_2 are sequestered to the mantle. **b.** Surface temperature evolution based on an 1-D atmospheric model.

METHODS

0.1. *Degassing of magma ocean*

Volatile partitioning between magma ocean and atmosphere—We solve for the degassing of the mantle based on volatile partitioning between the atmosphere and the mantle. The atmosphere and the melt phase at the surface of a magma ocean are assumed to be in equilibrium, so for each volatile component, the concentration in the surface magma, x_i, is calculated from the solubility at its partial pressure, P_i. When the mass of the melt-dominated layer is M_l, the following mass balance holds(Bower et al. 2019)

$$x_i \phi M_l + \frac{\mu_i}{\overline{\mu}} \frac{4\pi R_e^2}{g} P_i = m_i, \tag{1}$$

where ϕ is melt fraction at the surface of a magma ocean, μ_i is the molar mass of either H_2O or CO_2, $\overline{\mu}$ is the mean molar mass of the atmosphere, R_e is the Earth's radius, g is gravity, and m_i is the total mass of the volatile under consideration in the melt-dominated layer and the atmosphere (see Figure 1a). The first term indicates the volatile budget in the melt-dominated layer, where $x_s\phi$ is the bulk volatile concentration in a crystal-melt mixture of the melt-dominated layer. As a result of rapid convection, this bulk volatile concentration is assumed to be constant throughout the melt-dominated layer. For solubility, we adopt the parameterization of Blank and Brooker(Blank & Brooker 1994), and

$$P_{H_2O}(x_{H_2O}) = \left(\frac{x_{H_2O}}{6.8 \times 10^{-8}} \right)^{1.42} \tag{2}$$

and

$$P_{CO_2}(x_{CO_2}) = \left(\frac{x_{CO_2}}{4.4 \times 10^{-12}} \right) \tag{3}$$

are used for water and CO_2, respectively. Note that x_{H_2O} and x_{CO_2} are given in terms of mass fraction. Melt fraction at the surface ϕ is calculated from the surface temperature, which is estimated using a 1-D atmospheric model. The surface temperature, T_s, is a function of the atmospheric mass and composition and the net outgoing infrared radiation, and the outgoing radiation, F_{out}, is described as the sum of absorbed sunlight and convective heat flux(Zahnle et al. 1988; Solomatov 2007):

$$F_{out} = (1 - A)F_\odot + 0.089 \frac{k_T (T_m - T_s)}{d} Ra^{1/3}, \tag{4}$$

where A is the albedo, $F_\odot$ is solar flux (values discussed later in Atmospheric Model), k is thermal conductivity (4 W m^{-1} K^{-1}), T_m is mantle potential temperature, d is the depth of the melt-dominated layer, and Ra is the Rayleigh number of the melt-dominated layer. This value is set as $F_\uparrow$ at $\tau = 0$ in the atmospheric model.

At the beginning of the evolution, the entire mantle is assumed to be melt-dominated, and M_l is set to the mass of the entire mantle. The initial mass of volatile m_i is calculated from the initial volatiles concentration, which is assumed to be 0.04–0.1 wt% for water and 200–500 ppm for CO_2. As a magma ocean solidifies and the melt-dominated layer shrinks, the solid-dominated layer grows from the bottom of the mantle. Volatiles would be trapped in the porous melt phase of the solid-dominated layer, so when ΔM of the mantle solidifies to be solid-dominated and the melt-dominated layer shrinks by Δd, $\Delta M_l x_s \phi$ of volatiles would be removed from the volatile budget of the melt-dominated layer m_i:

$$m_i(d - \Delta d) = m_i(d) - \Delta M_l x_s \phi. \tag{5}$$

Equations (1–5) are solved as the melt-dominated layer solidifies until $d = 0$. The evolution of volatile budget is summarized in Extended Data Table 1.

Degassing of a magma ocean during the last phase of its solidification—When the melt-dominated layer disappears, the upper part of the mantle, while being rheologically solid, remains partially molten. When upward melt percolation is faster than solid-state convection, volatiles contained in the partially molten layer are expected to be released to the atmosphere (Figure 1b). As partial melt approaches the surface and solidifies, volatiles concentrate in the residual melt phase. Volatiles eventually exceed the saturation limit, and thus volatiles in the near-surface region would have degassed efficiently. We compare the timescales of melt percolation, t_{perc}, and convection, t_{conv}, to determine the depth where melt and volatiles can be extracted to the surface.

The timescale of melt percolation from a depth of D to the surface is given by

$$t_{\rm perc} = \frac{D}{v_{\rm perc}}, \tag{6}$$

where $v_{\rm perc}$ is percolation velocity(Dullien 1992),

$$v_{\rm perc} = \frac{d^2 g \Delta\rho}{150\eta_l} \frac{\phi^2}{1-\phi}. \tag{7}$$

Here d denotes the grain size of solid matrix, g is gravity, $\Delta\rho$ is density difference between the melt and solid phases, η_l is melt viscosity, and ϕ is melt fraction. For $d = 1$ mm^2, $g = 9.8$ m s^{-2}, $\Delta\rho = 400$ kg m^{-3}, and $\eta_l = 1$ Pa s,

$$t_{\rm perc} \sim 2.5 \left(\frac{D}{200\ {\rm km}}\right) \left(\frac{0.01}{\phi}\right)^2 \ {\rm Myr}. \tag{8}$$

The convective timescale is scaled using plate velocity as

$$t_{\rm conv} = \frac{D}{v_s} \sim 4.0 \left(\frac{D}{200\ {\rm km}}\right) \left(\frac{v_s}{5.0\ {\rm cm\ yr^{-1}}}\right) \ {\rm Myr}, \tag{9}$$

where v_s is plate velocity, whose formulation is described in the later section. These suggest that a partially molten layer with ϕ>0.01 likely becomes depleted in porous melt and thus volatiles.

The thickness of the partially molten layer is estimated from an adiabat with a melt fraction of 0.4 at the surface because the rapid Rayleigh-Taylor instability(Maurice et al. 2017; Miyazaki & Korenaga 2019) likely maintained an adiabatic temperature profile within the solid-dominated layer. A melt fraction of 0.4 marks the rheological transition of a partially molten medium(Abe 1993b; Solomatov 2007), and the Rhyolite-MELTS model(Gualda et al. 2012) is utilized to estimate melt fraction. For the chemically heterogeneous mantle with 0.1 wt% water, the melt-dominated layer would disappear at a potential temperature of ∼1625 °C, and the high-Mg# pyroxenite would be partially molten up to a depth of ∼4 GPa (Extended Data Figure 1). The chemically heterogeneous mantle consists of a mixture of iron-rich blobs and a high-Mg# pyroxenite matrix, so its average melt fraction should be 0.4 when the mantle starts to behave rheologcially as solid. The magma ocean model of ref. (Miyazaki & Korenaga 2019) suggests that the mass fraction of iron-rich blobs is about a quarter of the entire mantle, but because they are of small scale and not interconnected, the partial melt of iron-rich blobs is not considered to escape by percolation. We thus assume that volatiles contained in the top ∼4 GPa would be released to the atmosphere in Figure 2. It is noted that the melt-dominated layer would disappear at a potential temperature of ∼1600 °C for a pyrolitic mantle (Extended Data Figure 2). Therefore, the entire mantle is assumed to be rheologically solid at a potential temperature of 1600 °C for both chemically homogeneous and heterogeneous mantles, and these thermal structures are adopted as initial conditions for subsequent calculations.

We note that a small amount of degassing by episodic eruptions may also take place during the transition from magma ocean to solid-state convection. Our model assumes that the Rayleigh-Taylor instability efficiently cools the solid-dominated layer(Maurice et al. 2017; Miyazaki & Korenaga 2019), and the layer maintains an adiabatic thermal profile within the timescale of magma ocean solidification. Cooling, however, could be inhibited by tidal heating(Zahnle et al. 2015), and such heat may be released by episodic eruptions in addition to convective heat flux after the solidification of the mantle surface. Consequently, water degassing could be promoted, and ocean mass may increase rapidly. Yet, the interplay between tidal heating, cooling by the Rayleigh-Taylor instability, and melt percolation remains unconstrained, and future work is required to quantify the degree of degassing during this period. Episodic eruptions, however, would not affect the overall mode of mantle dynamics. Erupted melt would be recycled to the mantle by plate tectonics, and the rate of carbon sequestration is expected to remain unchanged from our model results.

0.2. *The composition of the chemically heterogeneous mantle*

The fractional crystallization of a magma ocean produces a structure dominated by the high-Mg# matrix with small iron-rich blobs (Figure 3a, Extended Data Figure 1d). Ref. (Miyazaki & Korenaga 2019) estimated that the ternary composition of the high-Mg# matrix is on average MgO 41.7 wt%, FeO 4.4 wt%, and SiO_2 53.9 wt%, whereas that

of iron-rich blobs is MgO 41.0 wt%, FeO 20.6 wt%, and SiO_2 38.3 wt%. The Mg# of the two components are ∼94 and ∼77, respectively, resulting in a difference in density and melting temperature. It is noted that iron-rich blobs make up ∼25% of the heterogeneous mantle, and the average composition of the mantle is consistent with the pyrolitic mantle.

The solidus of such a high-Mg# matrix is expected to be higher than that of a pyrolitic mantle, and we estimate the solidus temperature using the Rhyolite-MELTS model(Gualda et al. 2012). To predict the mineralogy of high-Mg# matrix, the Al_2O_3 and CaO contents are estimated using a partitioning model described in the following paragraph. Combining the results of the partitioning model with the ternary composition, we obtain an estimate of MgO 39.5 wt%, FeO 4.1 wt%, SiO_2 51.3 wt%, Al_2O_3 3.5 wt%, and CaO 1.5 wt% for the high-Mg# matrix, which results in a mineral assemblage of 70 wt% pyroxene, 25 wt% olivine, 5 wt% spinel at 1500 °C and 1.2 GPa. For Fe-rich blobs, a composition of MgO 37.8 wt%, FeO 19.0 wt%, SiO_2 35.3 wt%, Al_2O_3 3.7 wt%, and CaO 4.1 wt% is predicted, resulting in a mineral assemblage of 84 wt% olivine, 8 wt% of merwinite, 6 wt% of spinel, and 2 wt% of periclase. The melt fraction of the two components are shown in Extended Data Figure 1.

To predict the concentrations of Al_2O_3 and CaO, we construct an element partitioning model within the magma ocean, assuming that all newly crystals in the melt-dominated layer would stack at the base of the layer to form a rheologically rigid layer (Figure 1a). This is the same as crystal accumulation in the model of ref. (Miyazaki & Korenaga 2019). In a terrestrial magma ocean, crystals forming below the liquidus are predominantly bridgmanite under lower-mantle pressures, so at each time step, we calculate the amount of newly-formed bridgmanite and estimate the partitioning of Al_2O_3 and CaO between melt and bridgmanite. Bridgmanite would be incorporated in the growing rheologically rigid layer, which includes some amount of melt because the compaction of crystal-melt mixture can take place only slowly. The partitioning coefficients between melt and bridgmanite are estimated from the experimental results of refs. (Tronnes & Frost 2002) and (Corgne et al. 2005), and we adopt values of $D_{\mathrm{Al/Si}} = 0.78$ and $D_{\mathrm{Ca/Si}} = 0.16$.

The mantle is initially assumed to be entirely molten, and we run the model while newly formed bridgmanite is heavier than the remaining melt. The model of ref. (Miyazaki & Korenaga 2019) suggests that, when the depth of melt-dominated layer reaches 500 km, bridgmanite becomes lighter than the remaining melt and compositional fractionation ceases. The partitioning model indicates that the lower mantle, which eventually evolves into the high-Mg# matrix, would be depleted in CaO but shows little change in the Al_2O_3 content from the initial after the solidification (Extended Data Figure 4). We thus estimate that the high-Mg# matrix would have concentrations of Al_2O_3 3.6 ±0.7 wt% and CaO 1.51±0.11 wt%.

0.3. *Atmospheric evolution after the solidification of the mantle surface*

In our model, the removal of CO_2 from the atmosphere is governed by the formation of carbonates at ocean basins, which are sequestered to the mantle by subduction. At each time step, we remove CO_2 by carbonation formation, release H_2 by serpentinization, and update the surface temperature based on the new atmospheric pressure and composition. This procedure is repeated until all CO_2 in the atmosphere are sequestered to the mantle.

The timescale of CO_2 removal is assumed to be the same with that of ocean basins renewal, so the removal rate is proportional to the surface renewal rate and is inversely proportional to plate velocity. With the current plate construction rate(Parsons 1982) of 3.4 $\mathrm{km^2\ yr^{-1}}$, which corresponds to the average plate velocity of 5 $\mathrm{cm\ yr^{-1}}$, the entire ocean basin is renewed every 90 Myr. The amount of carbonate formed at the seafloor is estimated based on the assumption that Ca and Mg silicates in the top 500 m of oceanic crust reacted with CO_2(Zahnle et al. 2007), and we estimate that the Hadean seafloor contained ∼14 bar of CO_2, whereas current basaltic crust holds ∼2.5 bar of atmospheric CO_2. Details are discussed in the later section.

Plate velocity—When plate tectonics is operating, plate velocity, v_s, can be estimated from mantle heat flux, Q, as

$$v_s = v_{s,0}\left(\frac{Q}{Q_0}\frac{\Delta T_0}{\Delta T}\right)^2, \tag{10}$$

where ΔT is the temperature difference between the surface and mantle. The subscript 0 indicates the present-day values; $v_{s,0}$ is 5 $\mathrm{cm\ yr^{-1}}$, Q_0 is 38 TW, and ΔT_0 is 1350 K. Mantle heat flux Q is calculated based on the scaling of ref. (Korenaga 2010), which includes the effect of dehydration stiffening of depleted lithospheric mantle. Convective heat flux Q is given by

$$Q = Nu\frac{k_T A \Delta T}{L} \tag{11}$$

where Nu is the Nusselt number, A is the surface area of Earth, and L is the mantle depth. The Nusselt number Nu is calculated as(Korenaga 2010)

$$Nu = 2\left(\frac{Ra_i}{Ra_c}\right)^{1/3}\Delta\eta_L^{-1/3}, \tag{12}$$

where Ra_i is the internal Rayleigh Number, Ra_c is the critical Rayleigh number (≡1000), and $\Delta\eta_L$ is the lithospheric viscosity contrast. The internal Rayleigh number is defined as

$$Ra_i = \frac{\alpha\rho g\Delta T L^3}{\kappa\eta}, \tag{13}$$

where α is thermal expansivity, ρ is mantle density, and κ is thermal diffusivity. Mantle viscosity, η, changes with temperature with an activation energy, E, of 300 kJ/mol, and the reference viscosity is set to 10^{19} Pa s at 1350 °C. The lithospheric viscosity contrast $\Delta\eta_L$ changes with the thickness of depleted lithospheric mantle, h_m, as

$$\Delta\eta_L = \Delta\eta_{L,\mathrm{ref}}\exp\left[\ln(\Delta\eta)\min\left(1, \frac{h_m}{6h_{\mathrm{ref}}}\right)\right], \tag{14}$$

where $\Delta\eta_{L,\mathrm{ref}}$ is the reference viscosity contrast, $\Delta\eta$ is the viscosity contrast induced by mantle dehydration, and h_{ref} is the thickness of thermal boundary layer in the absence of dehydration stiffening, L/Nu_{ref}. The reference viscosity contrast $\Delta\eta_{L,\mathrm{ref}}$ is parameterized as(Korenaga 2010)

$$\Delta\eta_{L,\mathrm{ref}} = \exp\left(0.326\left(\frac{\mu}{\alpha\Delta T}\right)^{0.647}\theta\right), \tag{15}$$

where μ is an effective friction coefficient and θ is a nondimensionalized activation energy (known as the Frank-Kamenetskii parameter),

$$\theta = \frac{E\Delta T}{RT_p^2}, \tag{16}$$

where R is the universal gas constant and T_p is mantle potential temperature. To reproduce the present-day heat flux of 38 TW, we adopt $\Delta\eta = 100$ and $\mu = 0.025$. These values indicate that a dry mantle has a viscosity higher by 100 times than the present-day convecting mantle, and a mantle with a potential temperature of 1600 °C is 20 times less viscous than that of 1350 °C with the same degree of dehydration. It is noted that the rheology of the chemically heterogeneous mantle is expected to be similar to that of a pyrolitic mantle. The pyroxenite matrix contains 25% of olivine, which is a threshold for a phase to be interconnected, and thus its rheology would also be governed by olivine. Even if olivine grains are not interconnected, enstatite aggregates probably have similar viscosity to olivine aggregates under dislocation creep at temperatures expected for the Hadean mantle(Zhang et al. 2020).

The difference in plate velocity between the chemically homogeneous and heterogeneous mantles arises from h_m. Because a hotter mantle with the same composition would melt by a larger degree, the value of h_m for a pyrolitic mantle would be thicker than the present. To predict the thickness of dehydrated lithosphere, a fractional melting model is constructed based on the melting model of ref. (Katz et al. 2003). Assuming that a fraction of the partial melt escapes to the surface with each increment of new melting (see the caption of Extended Data Figures 1 and 2), the depleted lithospheric mantle would thicken to ∼140 km (4.5 GPa) for a mantle potential temperature of 1600 °C, from ∼60 km (2 GPa), which is the thickness for the present-day depleted lithospheric mantle (Extended Data Figure 2). On the other hand, the value of h_m for the chemically heterogeneous mantle is predicted to be ∼40 km based on the Rhyolite-MELTS model(Gualda et al. 2012), and the initial depth of melting has been corroborated with the pMELTS model(Ghiorso et al. 2002). Because the high-Mg# pyroxenite starts to melt at a shallower depth than a pyrolitic homogeneous mantle, and also because the partition coefficient of water between pyroxene and melt is larger than that between olivine and melt, we estimate that the mantle would not be completely dehydrated until 2 GPa. A value of 0.02 is adopted for water partitioning between the pyroxenite and melt, and 0.005 for partitioning between pyrolite and melt(Aubaud et al. 2004). It is noted that iron-rich blobs would melt at a depth deeper than 10 GPa (Extended Data Figure 1c), but the melting of blobs only creates locally depleted regions and thus is unlikely to affect the overall value of h_m.

A buoyancy constraint would further limit the plate velocity for a pyrolitic mantle(Davies 1992; Korenaga 2006) (Figure 3c). The thicknesses of buoyant basaltic crust and depleted lithospheric mantle increase as the mantle becomes

hotter, and thus the thermal boundary layer needs to grow sufficiently thick for plate to be negatively buoyant. The densities of oceanic crust and depleted lithospheric mantle are estimated using a model of ref. (Korenaga 2006), and to become negatively buoyant, the subduction age of plate is set to the critical age of lithosphere. Such a buoyancy constraint, however, does not apply for the case of chemically heterogeneous mantle. The melting of high-Mg# pyroxenite matrix would also produce buoyant oceanic crust at the surface, but its thickness is ∼4 km, 15% of crust formed under a pyrolitic (Figure 3b). Also, crust created by the melting of iron-rich blobs would act as a weight within a crust to promote subduction because iron-rich crust would have an Mg# of 56 and a density over 3500 kg m^{-3} (Extended Data Table 2). Fe-rich blobs start to melt at a deeper depth, so its crust would have an average thickness of ∼11 km. The crust of the chemically heterogeneous mantle would not be uniform, but the average crustal thickness is predicted to be ∼15 km, ∼70% of which originates from Fe-rich blobs. It is noted that the density of partial melt from iron-rich blobs is estimated to be 3000 kg m^{-3}, which is still lower than the high-Mg# matrix. Partial melt from iron-rich blobs would thus migrate upwards within the high-Mg# matrix. The density difference between iron-rich melt and the matrix is approximately four times smaller than that between partial melt from the matrix and the matrix itself, so these two kinds of partial melt may migrate upward without much mixing. The large fraction of the iron-rich crust may be situated below the high-Mg# crust, but some amount of iron-rich crust would be exposed at the surface, promoting H_2 and CH_4 production at the seafloor. Crustal composition is calculated by averaging the compositions of partial melt from the high-Mg# pyroxenite, and its mineral assemblage is estimated at 250 °C and 10 bar using Theriak-Domino(de Capitani & Petrakakis 2010) (Extended Data Table 2).

The thicknesses of crust and depleted lithospheric mantle are estimated based on an adiabatic temperature profile of the upper mantle. Adiabatic gradient is calculated using(Mckenzie 1984)

$$\left(\frac{dT}{dP}\right)_S = \phi\frac{\alpha_l T}{\rho_l c_p} + (1-\phi)\frac{\alpha_s T}{\rho_s c_p} - \frac{T\Delta S}{c_p}\left(\frac{d\phi}{dP}\right)_S, \tag{17}$$

where ϕ is melt fraction, α is thermal expansivity, ρ is density, c_p is specific heat per unit mass, and ΔS is entropy change upon melting. Subscripts l and s denote the melt and liquid phases, respectively. Values adopted for thermal expansivity are 3.0 and 4.6 $\times 10^{-5}$ K^{-1} for α_s and α_l, and, for density, ρ_l and ρ_s are taken to be 2900 and 3300 kg m^{-3}, respectively. We adopt 1000 J kg^{-1} K^{-1} for c_p and 300 J kg^{-1} K^{-1} for ΔS. The term $d\phi/dP$ in Equation (17) is determined so that changes in T and ϕ are consistent with both Equation (17) and the melting model. The effect of hydration on melting temperature depression is adopted from ref. (Katz et al. 2003) as

$$\Delta T(x_{H_2O}) = 0.43 \times x_{H_2O}^{0.75} \text{ K}, \tag{18}$$

where x_{H_2O} is the weight % of dissolved water content in the melt. Melting temperature decreases by a larger degree as melt fraction approaches zero, and the degree of decrease is largest at the solidus.

The evolution of mantle potential temperature T_p is solved using the following global heat balance equation(Christensen 1985):

$$C\frac{dT_p}{dt} = H - Q, \tag{19}$$

where C is the heat capacity of Earth (7×10^{27} J K^{-1}) and H is internal heat production by ^{238}U, ^{235}U, ^{232}Th, and ^{40}K. Internal heat production is calculated using a parameterization by ref. (Korenaga 2006). We assume an initial potential temperature of 1600 °C for both chemically homogeneous and heterogeneous mantles, as explained previously.

Mantle degassing by plate tectonics—Given that the current rate of plate construction(Parsons 1982) is 3.4 km^2 yr^{-1} and that the initial depth of mantle melting is ∼60 km, the processing rate of the present-day mantle is estimated to be $\sim 6.7 \times 10^{14}$ kg yr^{-1}, suggesting that it takes ∼6 Gyr to process the entire mantle. For the chemically heterogeneous mantle, plate velocity is faster by ∼9 times than the present, and the top 2–3 GPa would be dehydrated during the mantle upwelling (see Extended Data Figure 1). Therefore, the processing timescale of the chemically heterogeneous mantle is predicted to be shortened by a factor of 10–15 or to ∼400–600 Myr, suggesting that the entire mantle was mostly processed by the end of Hadean. Therefore, the mantle would have become mostly dry by then, and majority of the water budget would reside at the surface.

The operation of plate tectonics—For plate tectonics to operate, the negative buoyancy of the cold lithosphere should be large enough to bend subducting plates. It is noted that the term plate tectonics here refers to a mode of mantle convection that allows for the recycling of the surface layer, and plate kinematics could be different from modern-style plate tectonics. The criterion for plate tectonics is parameterized as(Korenaga 2010)

$$\Delta\eta_L \leq 0.25 Ra_i^{1/2} \equiv \Delta\eta_{L,crit}, \tag{20}$$

where $\Delta\eta_{L,crit}$ denotes the critical value for the operation of plate tectonics. For both chemically homogeneous and heterogeneous mantles, the lithospheric viscosity contrast is smaller than the critical value (Extended Data Figure 5), and thus plate tectonics is possible in the Hadean. Because water oceans were likely present at the surface, we consider that thermal cracking weakened the stiff lithosphere(Korenaga 2007) to reduce the value of effective friction coefficient to μ=0.02–0.03. The existence of oceans is the key to plate tectonics, because, if water oceans were absent in the Hadean, the value of μ increases to ∼0.8, resulting in a large lithospheric viscosity contrast. In such a case, the Hadean Earth would have operated under the stagnant lid mode, which lacks the recycling of the surface.

The fate of iron-rich blobs—With a mantle potential temperature of 1600 °C, the high-Mg# pyroxenite matrix would experience ∼27% melting, whereas iron-rich blobs would melt up to ∼43% when blobs maintain a thermal equilibrium with the pyroxenite matrix (Extended Data Figure 1c). Iron-rich blobs are predominantly consisted of olivine, and the partial melt would be further enriched in iron. The Rhyolite-MELTS model(Gualda et al. 2012) predicts that such a crust has a composition of MgO 16.0 wt%, FeO 22.9 wt%, SiO_2 39.2 wt%, Al_2O_3 9.2 wt%, and CaO 12.6 wt%, resulting in an Mg# of 56 and a crustal density higher than 3500 kg m^{-3} (Extended Data Table 2). The melt density of partial melt from iron-rich blobs is 3000 kg m^{-3}, which is still lower than the density of the pyroxenite matrix, so the iron-rich melt would migrate upward.

The preexisting lithological heterogeneities (high-Mg# matrix and iron-rich blobs) as well as the newly generated heterogeneities (crustal products and solid residues) would eventually be homogenized as the mantle evolves, but timescale for mixing depends on many uncertain parameters(Tackley 2015). For example, the subducted iron-rich crust would be denser than ambient mantle, so it may stay longer in the lower mantle without being homogenized with the entire mantle(Davies 2006). It is not unrealistic to expect that the initial heterogeneity likely survived until the end of the Hadean.

Atmospheric model—The surface temperature is calculated using a 1-D radiative-convective atmosphere model of ref. (Nakajima et al. 1992). This model assumes that the atmosphere is gray to outgoing infrared radiation but transparent to incoming solar visible radiation. The atmosphere consists of two layers, stratosphere and troposphere, where temperature in the stratosphere is controlled by radiative equilibrium, whereas convective heat transport from the bottom governs the thermal structure in the troposphere. The atmosphere is assumed to be plane-parallel and is transparent to solar radiation, but opaque to infrared radiation regardless of the wavelength. For simplicity, the effects of clouds are neglected in our model.

We assume that the early Earth atmosphere contains 1 bar of N_2 with a varying mixture of CO_2 and H_2O, which are determined based on the partitioning of volatiles between a magma ocean and the atmosphere. Sulfur and chloride volatiles may have also contributed to the greenhouse effect(Johnson et al. 2008), but its effect is likely to be smaller compared to that created by a thick atmosphere of CO_2 and H_2O. A solar constant 30% smaller than the present is adopted to account for the faint young Sun, and the planetary albedo is fixed at 0.3. The hydrodynamic escape of volatiles is not included in this model for simplicity, although its effect would be significant for the case of homogeneous mantle, whose evolutionary timescale exceeds 1 Gyr.

The temperature structure in the stratosphere is calculated using radiative equilibrium, which can be written as a function of optical thickness, τ:

$$\sigma_B T(\tau)^4 = \frac{1}{2} F_{\rm net} \left(\frac{3}{2}\tau + 1 \right), \tag{21}$$

where σ_B is the Stefan-Boltzmann constant and $F_{\rm net}$ is the net infrared flux emitted from the top of the atmosphere. Upward, $F_\uparrow$, and downward radiation fluxes, $F_\downarrow$, are also calculated as

$$F_\uparrow(\tau) = \frac{1}{2} F_{\rm net} \left(\frac{3}{2}\tau + 2 \right), \tag{22}$$

$$F_\downarrow(\tau) = \frac{1}{2} F_{\rm net} \left(\frac{3}{2}\tau \right). \tag{23}$$

Optical thickness τ is defined so that it increases towards the Earth's surface:

$$\tau(z) = -\int_{\infty}^{z} \kappa \rho_g dz, \tag{24}$$

where κ denotes the Rosseland mean opacity. Opacity κ depends on the atmospheric concentrations of greenhouse gases, and for the atmosphere which has a molar fraction of x_i of gas species i, κ is given by

$$\kappa = \frac{1}{\overline{\mu}} \sum_i \kappa_i x_i \mu_i, \tag{25}$$

where $\overline{\mu}$ is the mean molar mass of gas, κ_i and μ_i are the Rosseland mean opacity and molar mass, respectively, of species i. For opacity, we use 10^{-2} for H_2O, 1.3×10^{-4} for CO_2(Abe & Matsui 1985), and 0 for N_2, assuming N_2 is transparent to infrared radiation. The composition of the atmosphere is assumed to be uniform in the stratosphere.

In the troposphere, the thermal structure is controlled by the moist adiabatic lapse rate, which is given by

$$\left(\frac{dT}{dP}\right) = \frac{\overline{\mu}}{\rho_g c_p} \frac{1 + \dfrac{qL}{RT}}{1 + \dfrac{qL^2}{c_p R T^2}}, \tag{26}$$

where ρ_g is the mean gas density, q is water mixing ratio, L is the latent heat of the water, and R is the universal gas constant. Water mixing ratio q is set to be saturated, which is likely in a CO_2 dominated atmosphere, and is obtained from the water phase diagram.

The tropopause, a boundary between the stratosphere and troposphere, is determined as a height that the radiation energy is balanced. The upward radiation flux emitted from the troposphere can be calculated as

$$F_{\uparrow}(\tau) = -\sigma_B T^4 + \int_{\tau_b}^{\tau} e^{-(\tau' - \tau)} \frac{d}{d\tau'} \left(\sigma_B T(\tau')^4\right) d\tau', \tag{27}$$

where τ_b is the optical depth at the bottom of the atmosphere. We assume that the upward flux at the ground is the blackbody radiation of the ground temperature ($F_{\uparrow,\mathrm{surf}} = -\sigma_B T_{\mathrm{surf}}^4$). At the optical depth of the tropopause, τ_p, the values of $F_{\uparrow}(\tau_p)$ calculated from Equations (22) and (27) should be identical to satisfy the energy balance. We search for the profiles of temperature and water vapor content that agree with energy conservation. The temperature and the water vapor mixing ratio are smoothly connected at the tropopause.

0.4. *Carbon sequestration*

The alteration of oceanic crust—The alteration of upper oceanic crust is a major source of carbon entering subduction zones(Dasgupta & Hirschmann 2010; Kelemen & Manning 2015), and its flux size was likely to be larger in the Hadean. The upper 500 m of oceanic crust is highly porous, and considering rapid kinetics under high surface temperatures, the porous layer would have efficiently reacted with the seawater. Under an atmospheric pressure over 100 bar, the solubility of CO_2 in water is elevated by more than an order of magnitude(Diamond & Akinfiev 2003), so reactions between silicates within in the upper oceanic and CO_2 would be promoted as well. Ca- and Mg-silicates are thermodynamically susceptible to carbonation under a thick CO_2 atmosphere(Sleep et al. 2001), so we estimate CO_2 uptake by these silicates within in the upper oceanic crust.

The basis for efficient carbonation is that the Hadean seafloor was supersaturated with respect to carbonate minerals. The modern oceans become undersaturated below 3500–5000 m(Peterson 1966; Andersson 2014), but the carbonate compensation depth was likely to be deeper in the Hadean owing to two main factors(Andersson 2014): (1) a higher surface temperature due to greenhouse effect and (2) an initially shallower ocean because of the greater water content of the mantle. The amount of water at the surface is estimated to have been less than 10% of the present day in the Hadean (Figure 2), so ocean depth was likely shallower than 500 m. Even with an atmospheric pressure of ∼200 bar, pressure at the seafloor would be lower than ∼250 bar. Higher temperatures and lower pressures inhibit the dissolution of carbonates(Andersson 2014) and thus promote carbonate alteration of the oceanic crust. It is noted that a lower pH due to a thicker CO_2 atmosphere would not be a limiting factor for carbonation. The relative proportion of carbonate ion to the total carbon amount decreases significantly with a lower pH, but carbonate ion concentration

would still be larger than the present, or at least remain the same, because the total amount of carbon in the seawater is substantially larger. The actual carbonate ion concentration remains uncertain due to limited experimental data, but the carbonation of oceanic crust is expected to be efficient as long as carbonate ion is present and dissolution is inhibited.

The crust of the chemically heterogeneous mantle would be a mixture of those derived from high-Mg# pyroxenite and Fe-rich blobs, and both components have a large capacity of storing CO_2. Because the formation of carbonates is thermodynamically favorable for Ca- and Mg-silicates under a high CO_2 concentration(Sleep et al. 2001), we assume that all Ca- and Mg-silicates are used to form carbonates. The crust formed from high-Mg# pyroxenite and Fe-rich blobs both contain ∼10 wt% of CaO (Extended Data Table 2), so when all Ca-silicates are carbonated, the upper crust would store up to 3.5×10^{19} kg or ∼7 bar of CO_2. This is 2.7 times of the present-day Earth, where the top 500 m of basaltic crust contains ∼3.0 wt% of CO_2, equivalent to 1.3×10^{19} kg or ∼2.5 bar of CO_2(Alt & Teagle 1999). Mg-silicates, which mostly exist as olivine, orthopyroxene, or clinopyroxene (Extended Data Table 2), are also prone to carbonation(Kelemen et al. 2011), among which olivine has the highest rate of carbonation. The crust of the heterogeneous mantle contains 16–22% of MgO, depending on the relative proportion of high-Mg# and Fe-rich source crusts, so even with a lower bound estimate, the upper crust could contain up to 8.0×10^{19} kg or ∼15.4 bar of CO_2. This suggests that the seafloor could contain up to ∼22 bar of CO_2 at one time. Fe-silicates are not considered as a sink for CO_2 because they are more likely to be oxidized to produce H_2.

Carbonates created by hydrothermal alteration would mostly be delivered to the deep mantle under a rapid plate motion. The loss of carbonates in the plate is determined by two factors: (1) the stability of carbonates under a hotter deeper region and (2) the solubility of carbon to water released from the decomposition of hydrous minerals(Kelemen & Manning 2015). The stability of carbonates within oceanic crust depends on the P-T path of subducting plates, and carbonates are considered to be stable under majority of the modern subduction settings(Dasgupta & Hirschmann 2010). This is also likely to be the case for the Hadean subduction zones. Although the surface temperature and mantle potential temperature are both hotter by ∼200 K, the P-T path of subducting slab would remain similar to the present-day young subduction zones (Extended Data Figure 3). For the chemically heterogeneous mantle, the rapid plate velocity would allow the slab to be delivered to the deeper region without substantial heating from the surrounding mantle. A pyrolitic homogeneous mantle would have slower plate velocity, but because oceanic plates are older and thus colder, the slab temperature at the deeper region would be similar to that of the heterogeneous mantle. The actual geotherm could vary among different subduction settings even with the same age and plate velocity(Syracuse et al. 2010), so the temperature of some slab surfaces may reach the solidus of carbonate melting(Dasgupta et al. 2004). On average, however, the subducting slab is expected to remain colder than the carbonate solidus (Extended Data Figure 3), recycling only a fraction of subducting carbonates back to the surface. Moreover, some fraction of the extracted carbon would be stored in mantle lithosphere and continental crust(Kelemen & Manning 2015), the latter of which would have been created by the melting of hydrated subducted materials. Modeling the thermal structure of subduction zones is still subject to large uncertainties as a number of important assumptions are involved, and in this study, we tentatively estimate that 50% of subducted carbonates return to the surface for both pyrolitic and heterogeneous mantles (Figure 4). Whereas the timescale of carbon sequestration would be longer for less efficient carbon subduction, it would always be shorter by an order of magnitude for the case of the heterogeneous mantle.

The loss of carbon may also take place by the dissolution of carbonates to fluid released by serpentine. The Hadean plates, however, are expected to contain ∼9 times more carbonates than the present-day oceanic crust, and thus it is unlikely for all carbonates to be dissolved. When the top 500 m of oceanic crust contains ∼10 wt% of water, the maximum amount of CO_2 that could dissolve into serpentinite-driven fluid is 4.4×10^{17} kg, which is less than 1% of total carbonates in oceanic crust. Here, we assume that serpentinize releases water at ∼3 GPa and the solubility of carbonates to fluid is 10^4 ppm(Kelemen & Manning 2015). The amount of water in the underlying crust and mantle is predicted to be limited due to high confining pressure(Korenaga 2017; Miller et al. 2021). Considering that the top 30 km includes 0.1 wt% of water, the additional dissolution of CO_2 would be less than 1% of total carbonates in the upper crust. Therefore, the amount of recycled carbon through dissolution is expected to be negligible in the Hadean.

The composition and redox of the atmosphere—For both chemically homogeneous and heterogeneous mantles, crust has a higher MgO content and thus forms more olivine. The dissolution of olivine is efficient compared to other silicate

minerals, and thus following reactions are likely to occur:

$$3Fe_2SiO_4 + 2H_2O \rightarrow 2Fe_3O_4 + 3SiO_2 + 2H_2, \tag{28}$$

$$3Mg_2SiO_4 + SiO_2 + 4H_2O \rightarrow 2Mg_3Si_2O_5(OH)_4, \tag{29}$$

where each reaction represents oxidation of ferrous iron and serpentinization of forsterite. We assume that all fayalite would be oxidized to form magnetite by Reaction (28). The serpentinization of forsterite would consume SiO_2 and thus promotes the oxidation of iron and the carbonation of other minerals.

The amount of hydrogen production differs between the chemically homogeneous and heterogeneous mantles because of their difference in mineral assemblage of the seafloor. Crust with a lower Mg# contains more iron and thus produces more H_2. Following the stoichiometry of reactions, 0.07 mol of H_2 is estimated to be released to the atmosphere per 1 mol of olivine in the case of the homogeneous pyrolitic mantle, whereas 0.04 mol of H_2 is released for the chemically heterogeneous mantle. The H_2 production rate, however, is higher for the chemically heterogeneous mantle because the seafloor is renewed at a rate ∼10 times faster than the homogeneous pyrolitic mantle (Figure 4a).

The composition of the atmosphere is calculated using Gibbs free energy minimization, the implementation of which is described in ref. (Miyazaki & Korenaga 2017). We calculate equilibrium under temperature and pressure conditions at the bottom of the atmosphere. CO_2, CO, CH_4, H_2O, and H_2 are considered are possible species. In reality, the atmospheric composition is affected by photochemical reactions. Such an effect, however, is not included because our aim is to provide a zeroth-order estimate on the change in redox state with active carbonation and serpentinization.

Subduction geotherms—The P-T path of Extended Data Figure 3 is calculated using the model of ref. (Wirth & Korenaga 2012). The age of subducting plate is assumed to be 10 Myr with a slab dip angle of 45°, but the angle does not have a significant influence on the geotherm. For an activation energy for viscosity, the value of 300 kJ mol^{-1} is adopted. Because the model assumes an incompressible fluid, the modeled potential temperature is converted to the actual value using an adiabatic gradient of 0.5 K km^{-1}.

Data Availability—All relevant data are provided in the paper. Codes to reproduce the results are available at https://github.com/yoshi-miyazaki/Hadean-evolution/. Gibbs energy minimization code is available at https://github.com/yoshi-miyazaki/GibbsE-minimization/.

Acknowledgments—This work was sponsored by the U.S. National Aeronautics and Space Administration under Cooperative Agreement No. 80NSSC19M0069 issued through the Science Mission Directorate and the National Science Foundation under grant EAR-1753916. This work was also supported in part by the facilities and staff of the Yale University Faculty of Arts and Sciences High Performance Computing Center. Y.M. was supported by the Stanback Postdoctoral Fellowship from Caltech Center for Comparative Planetary Evolution. The authors thank Norman Sleep and Marc Hirschmann for providing constructive comments, which were helpful to substantially improve the accuracy of the manuscript.

Author Contributions—Y.M. and J.K. designed the study, discussed the results, and wrote the manuscript. Y.M. performed calculations.

Competing Interests—The authors declare no competing financial interests.

Correspondence—Correspondence and requests for materials should be addressed to Y.M. (email: ymiya@caltech.edu).

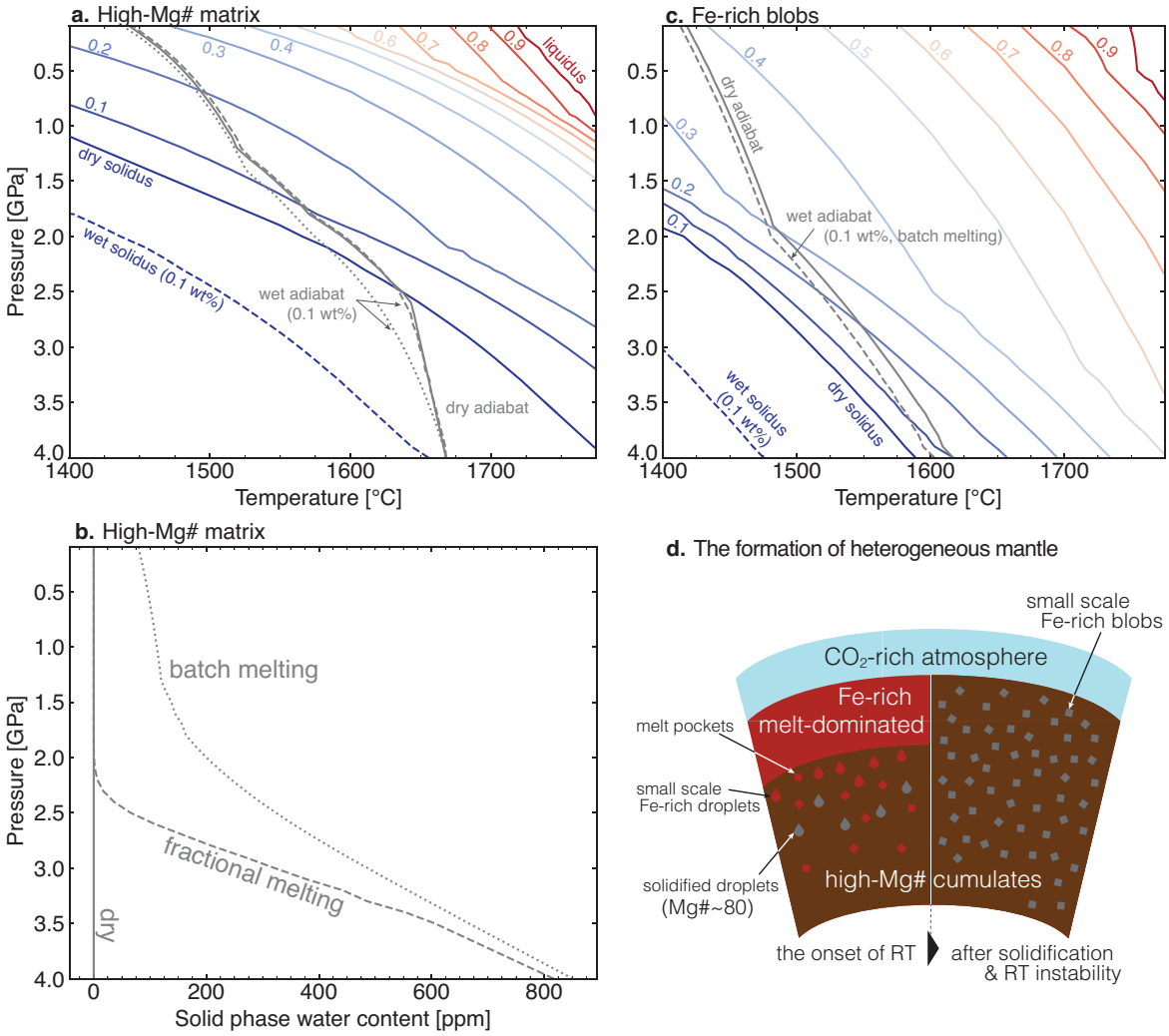

Extended Data Figure 1. The thermal structure of the chemically heterogeneous mantle plotted together with contours of melt fraction. a–c. Melt fraction is shown for two components of the mantle, **a.** high-Mg# pyroxenite matrix and **c.** Fe-rich blobs, and **b.** water content remaining in the solid phase of the high-Mg# matrix. The melt fractions of high-Mg# matrix and Fe-rich blobs are estimated using the Rhyolite-MELTS model(Gualda et al. 2012). The dry (gray solid) and wet (0.1 wt%; gray dashed) adiabats are calculated with a potential temperature of 1600 °C, using Equation (17). For the wet adiabat of the high-Mg# matrix, two modes of melting are considered, batch (dotted) and fractional (dashed), and for the latter, we assume that 90% of melt would escapes from the mantle for every 0.1 GPa of ascent when the degree of melting is greater than 1%. The fraction of melt escaping the system is insensitive to the thickness of complete dehydration, and values between 10% and 99.9% would yield a thickness within 0.1 GPa of what is predicted in this figure. **d.** Schematic illustration of the compositional structure of the mantle during and after the solidification of a magma ocean under fractional crystallization. The mantle experiences global-scale chemical stratification, leaving an Fe-rich layer near the surface. Such stratification is subject to the Rayleigh-Taylor (RT) instability, resulting in the dripping-like descent of Fe-rich materials. This period corresponds to Figure 1a. These droplets would solidify as they sink through the mantle (left) and be mixed with high-Mg# cumulates. When the surface becomes rheologically solid (Figure 1b), the mantle would have a structure with small-scale chemical heterogeneity, embedded in high-Mg# matrix (right).

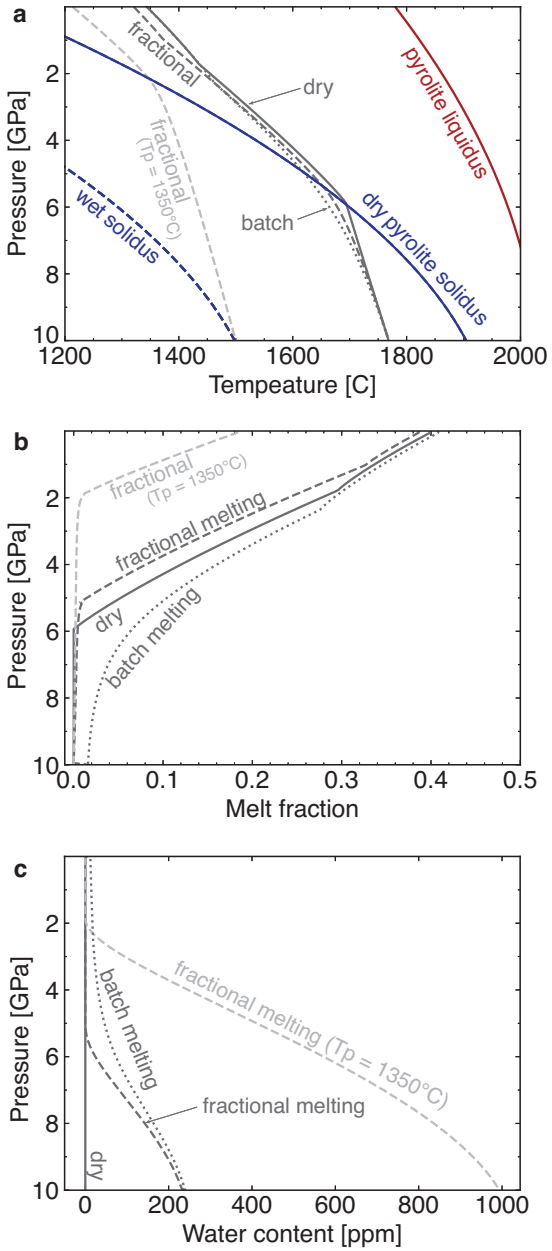

Extended Data Figure 2. Thermal structure of a pyrolitic (chemically homogeneous) mantle when a melt-dominated layer disappears. The figure describes when the entire mantle starts to behave rheologically as solid, which corresponds to a potential temperature of ∼1600 °C. The profiles of **a.** temperature, **b.** melt fraction, and **c.** water content are shown for both dry (gray solid) and wet (0.1 wt%; gray dotted and dashed) mantles, together with the solidus (blue) and liquidus of pyrolite (red). The solidus of a wet mantle (blue dashed) is estimated using Equation (18) and a melt/mineral partitioning coefficient of D=0.005. Two modes of melting are considered for the wet mantle, batch (dotted) and fractional (dashed). Temperature profiles would be adiabatic as a result of the Rayleigh-Taylor instability, and melt fraction is estimated using a model of ref. (Katz et al. 2003) with the mass fraction of clinopyroxene of 19 wt%. For fractional melting, we assume that 90% of melt would escapes from the mantle for every 0.1 GPa of ascent when the degree of melting is greater than 1%.

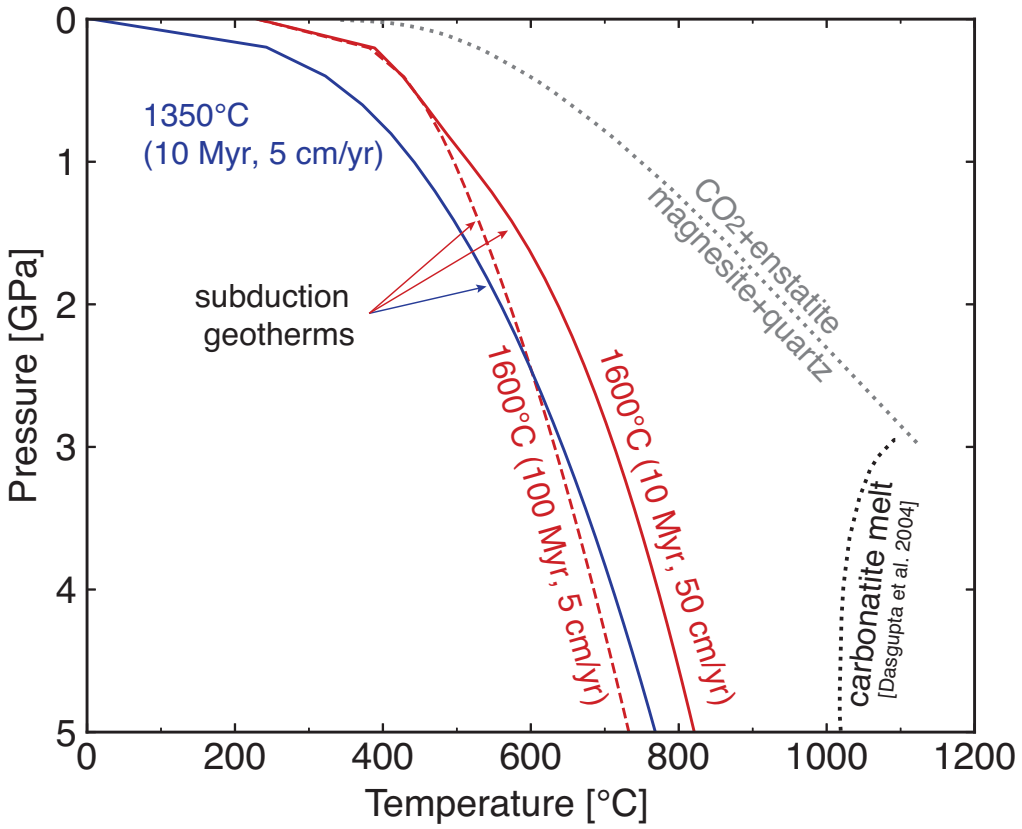

Extended Data Figure 3. The subduction geotherm during the Hadean with the stability field of carbonantes. *P-T* paths are calculated assuming a dip angle of 45° using the model of ref. (Wirth & Korenaga 2012) (see Methods for details). We consider (1) a mantle potential temperature of 1350 °C with a plate age of 10 Myr, a velocity of 5 cm yr^{-1}, and a surface temperature of 0 °C (blue), (2) a potential temperature of 1600 °C with a plate age of 10 Myr, a velocity of 50 cm yr^{-1}, and a surface temperature of 230 °C (red solid), and (3) a potential temperature of 1600 °C with a plate age of 100 Myr, a velocity of 5 cm yr^{-1}, and a surface temperature of 230 °C (red dashed), representing the present-day young slab, the Hadean slab of the chemically heterogeneous mantle, and that of a homogeneous pyrolitic mantle, respectively. *P-T* paths of the heterogeneous and homogenous mantles are similar because rapid plate motion mitigates the heating of the slab from the surrounding mantle. The solidus of carbonate melt is adopted from ref. (Dasgupta et al. 2004) (black dotted), and the decomposition of magnesite under the presence of quartz is calculated using Theriak-Domino(de Capitani & Petrakakis 2010) (gray dotted).

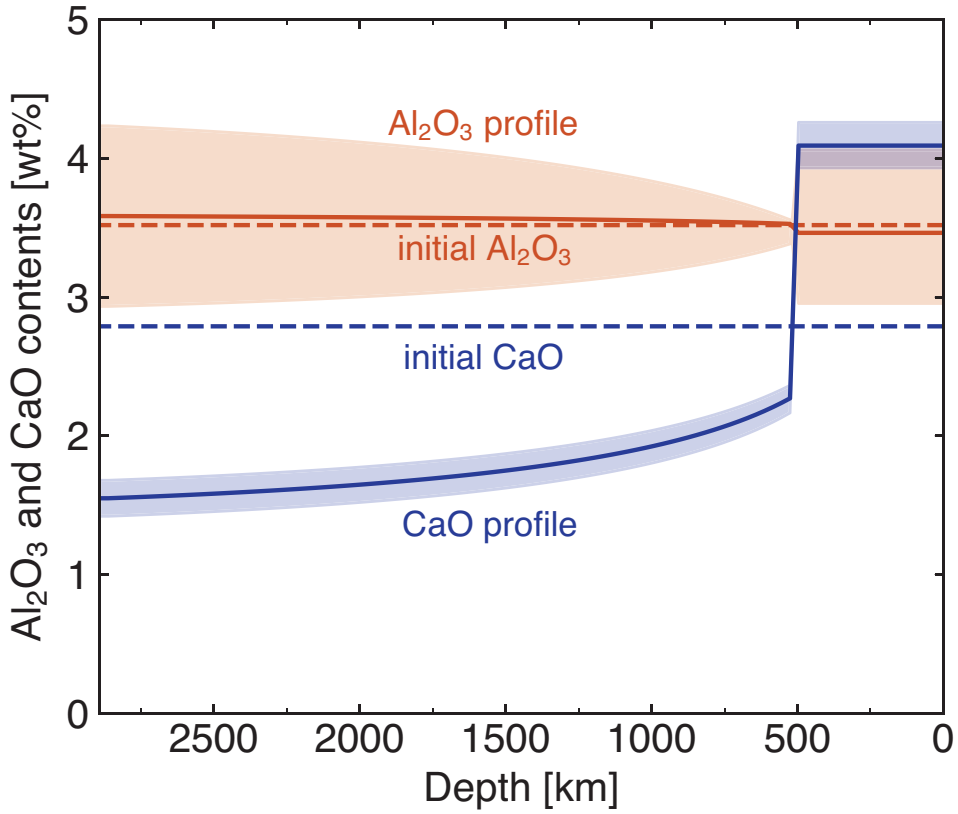

Extended Data Figure 4. The profiles of Al_2O_3 (red) and CaO (blue) contents after magma ocean solidification. Profiles before the onset of small-scale Rayleigh-Taylor instabilities are shown. The top 500 km of the mantle becomes the source for iron-rich blobs, whereas the lower mantle composition corresponds to the high-Mg# matrix in the main text. We assume that newly formed crystals in the magma ocean would stack at the base of the melt-dominated layer (Figure 1a). Initial concentrations of Al_2O_3 3.5 wt% and CaO 2.8 wt%(Lyubetskaya & Korenaga 2007) are assumed (dashed lines), and partitioning coefficients between melt and bridgmanite are calculated from the experimental results of Tronnes and Frost(Tronnes & Frost 2002) and Corgne et al.(Corgne et al. 2005) Shaded areas represent uncertainties, which are calculated using partitioning coefficients 30% larger and smaller values than the mean estimated values ($D_{\mathrm{Al/Si}} = 0.78$ and $D_{\mathrm{Ca/Si}} = 0.16$).

	CO_2 [kg]		H_2O [kg]	
	surface	interior	surface	interior
The beginning of magma ocean	9.0×10^{20}	3.0×10^{20}	4.6×10^{19}	4.0×10^{21}
After the solidification	9.3×10^{20}	2.7×10^{20}	1.1×10^{20}	3.9×10^{21}
The end of Hadean	1.7×10^{19}	1.2×10^{21}	4.2×10^{21}	0
Present-day	1.7×10^{17}	1.2×10^{21}	1.4×10^{21}	2.8×10^{21}

Extended Data Table 1. The evolution of CO_2 and H_2O budgets. The initial CO_2 and H_2O concentrations are set to 300 pm and 0.1 wt%, respectively, to calculate values in this Table. Estimates for the magma ocean stage are taken from Figure 2, which is calculated based on the volatile partitioning model. Because of rapid plate tectonics, most CO_2 in the atmosphere was likely sequestered to the mantle, whereas remaining water in the mantle was degassed by the end of the Hadean (see Methods for details). The present-day values are adopted from refs. (Hirschmann & Dasgupta 2009) and (Korenaga et al. 2017).

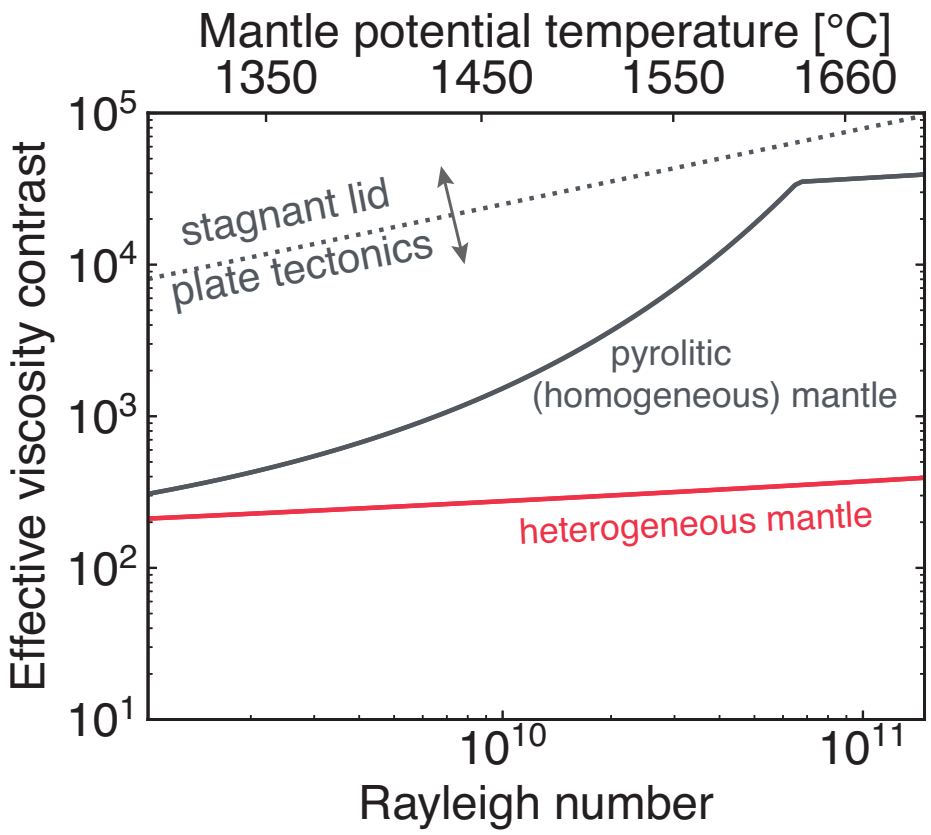

Extended Data Figure 5. Effective viscosity contrast across the lithosphere and the criteria for plate tectonics. Effective viscosity contrast is shown (Equation (14)) as a function of the internal Rayleigh number, together with the corresponding mantle potential temperature. The thickness of depleted lithospheric mantle h_m in Equation (14) is different between chemically homogeneous (gray) and heterogeneous mantles (red), and the values of h_m are shown in Figure 3b. The criteria for plate tectonics ($\Delta\eta_{L,crit}$ in Equation (20)) is also plotted with a dotted line.

	SiO_2	MgO	FeO	Al_2O_3	CaO [wt%]	olivine	opx	cpx	feldspar	others [wt%]	density [kg/m^3]
High-Mg# crust*	43.6	21.5	5.3	18.9	10.7	20.9	21.5	26.9	18.5	12.1§	3010#
High-Mg# DLM	52.0	41.5	4.2	1.8	0.5	33.4	64.7	1.9	-	-	3120
High-Mg# pyroxenite	51.3	39.5	4.1	3.5	1.5	24.9	69.8	-	-	5.2§	3130
Iron-rich crust†	39.2	16.0	22.9	9.2	12.6	38.9	-	46.3	1.5	13.4‖	3570⋆
Iron-rich DLM	33.9	45.5	18.1	1.61	1.02	85.2	-	-	-	14.8‖	3340
Iron-rich blobs	35.3	37.8	19.0	3.7	4.1	84.0	-	-	-	16.0‖	3350
Modern MORB‡	50.47	7.58	10.43	14.7	9.4	9.3	11.6	24.1	51.4	3.5¶	3030

Extended Data Table 2. Compositions of high-Mg# pyroxenite, iron-rich blobs, and their differentiated components. Mineral proportions and densities are calculated using Theriak-Domino(de Capitani & Petrakakis 2010) under 250 °C and 10 bar for crustal components and 1500 °C and 1.2 GPa for mantle components. DLM indicates depleted lithospheric mantle, which is calculated as the depleted residue of partial melting.

* From the partial melt of pyroxenite at 1570°C and 1.8 GPa with 11 % melting.

† From the partial melt of iron-rich blob at 1520 °C and 2.3 GPa with 28 wt% melting.

‡ From ref. (Gale et al. 2013). The total of oxides is lower than 100 % because other minor oxides, including Na_2O and TiO_2, are not shown here.

§ The high-Mg# pyroxenite contains spinel, whereas crust contains corundum.

‖ Iron-rich blobs and its depleted reservoir include merwinite, spinel, and periclase, whereas iron-rich crust only contains spinel.

¶ Mid-ocean ridge basalt contains ilmenite as a Ti-bearing phase.

Before crystallization, the melt density of partial melt from the high-Mg# pyroxenite is 2660 kg m^{-3}. The melt density is calculated using the Rhyolite-MELTS model(Gualda et al. 2012) at a temperature of 1500 °C and 10 bar. Under a mantle condition of 1500 °C and 1.2 GPa, the density increases to 3180 kg m^{-3}, and it is likely to be heavier than the ambient mantle.

⋆ Before crystallization, the melt density of partial melt from iron-rich blobs is 3000 kg m^{-3}. The melt would thus migrate upwards within the pyroxenite matrix. Its density under the mantle condition is estimated to be 3440 kg m^{-3}.

REFERENCES

Abe, Y. 1993a, Lithos, 30, 223, doi: 10.1016/0024-4937(93)90037-D

—. 1993b, Geophysical Monograph 74, 14, 41

Abe, Y., & Matsui, T. 1985, Journal of Geophysical Research, 90, C545, doi: 10.1029/jb090is02p0c545

Alt, J. C., & Teagle, D. A. 1999, Geochimica et Cosmochimica Acta, 63, 1527, doi: 10.1016/S0016-7037(99)00123-4

Andersson, A. J. 2014, in Treatise on Geochemistry, Second Edition, ed. H. D. Holland & K. Turekian, Vol. 8 (Elsevier), 519–542, doi: 10.1016/B978-0-08-095975-7.00619-7

Aubaud, C., Hauri, E. H., & Hirschmann, M. M. 2004, Geophysical Research Letters, 31, L20611, doi: 10.1029/2004GL021341

Blank, J. G., & Brooker, R. A. 1994, in Reviews in Mineralogy and Geochemistry, ed. M. R. Carrol & J. R. Holloway (Mineralogical Society of America), 157–186

Bower, D. J., Kitzmann, D., Wolf, A. S., et al. 2019, Astronomy and Astrophysics, 631, A103, doi: 10.1051/0004-6361/201935710

Bradley, D. C. 2008, Earth-Science Reviews, 91, 1, doi: 10.1016/j.earscirev.2008.08.001

Canup, R. M., & Asphaug, E. 2001, Nature, 412, 708

Catling, D. C., & Zahnle, K. J. 2020, Science Advances, 6, eaax1420, doi: 10.1126/sciadv.aax1420

Christensen, U. R. 1985, Journal of Geophysical Research, 90, 2995

Corgne, A., Liebske, C., Wood, B. J., Rubie, D. C., & Frost, D. J. 2005, Geochimica et Cosmochimica Acta, 69, 485, doi: 10.1016/j.gca.2004.06.041

Dasgupta, R., & Hirschmann, M. M. 2010, Earth and Planetary Science Letters, 298, 1, doi: 10.1016/j.epsl.2010.06.039

Dasgupta, R., Hirschmann, M. M., & Withers, A. C. 2004, Earth and Planetary Science Letters, 227, 73, doi: 10.1016/j.epsl.2004.08.004

Davies, G. F. 1992, Geology, 20, 963, doi: 10.1130/0091-7613(1992)020⟨0963:OTEOPT⟩2.3.CO;2

—. 2006, Earth and Planetary Science Letters, 243, 376, doi: 10.1016/j.epsl.2006.01.053

de Capitani, C., & Petrakakis, K. 2010, American Mineralogist, 95, 1006, doi: 10.2138/am.2010.3354

Deng, J., Du, Z., Karki, B. B., Ghosh, D. B., & Lee, K. K. 2020, Nature Communications, 11, 2007, doi: 10.1038/s41467-020-15757-0

Diamond, L. W., & Akinfiev, N. N. 2003, Fluid Phase Equilibria, 208, 265, doi: 10.1016/S0378-3812(03)00041-4

Dullien, F. A. L. 1992, Porous media: Fluid transport and pore structure, 2nd edn. (San Diego: Academic Press)

Elkins-Tanton, L. T. 2008, Earth and Planetary Science Letters, 271, 181, doi: 10.1016/j.epsl.2008.03.062

Gale, A., Dalton, C. A., Langmuir, C. H., Su, Y., & Schilling, J.-G. 2013, Geochemistry, Geophysics, Geosystems, 14, 489, doi: 10.1029/2012GC004334

Ghiorso, M. S., Hirschmann, M. M., Reiners, P. W., & Kress, V. C. 2002, Geochemistry, Geophysics, Geosystems, 3, doi: 10.1029/2001GC000217

Gualda, G. A., Ghiorso, M. S., Lemons, R. V., & Carley, T. L. 2012, Journal of Petrology, 53, 875, doi: 10.1093/petrology/egr080

Hamano, K., Abe, Y., & Genda, H. 2013, Nature, 497, 607, doi: 10.1038/nature12163

Harrison, T. M. 2009, Annual Review of Earth and Planetary Sciences, 37, 479, doi: 10.1146/annurev.earth.031208.100151

Herzberg, C., Condie, K., & Korenaga, J. 2010, Earth and Planetary Science Letters, 292, 79, doi: 10.1016/j.epsl.2010.01.022

Hier-Majumder, S., & Hirschmann, M. M. 2017, Geochemistry, Geophysics, Geosystems, 18, 3078, doi: 10.1002/2017GC006937

Hirschmann, M. M. 2012, Earth and Planetary Science Letters, 341-344, 48, doi: 10.1016/j.epsl.2012.06.015

Hirschmann, M. M., & Dasgupta, R. 2009, Chemical Geology, 262, 4, doi: 10.1016/j.chemgeo.2009.02.008

Hirth, G., & Kohlstedt, D. L. 1996, Earth and Planetary Science Letters, 144, 93, doi: 10.1016/0012-821x(96)00154-9

Jain, C., Korenaga, J., & Karato, S.-i. 2019, Journal of Geophysical Research: Solid Earth, 124, 310, doi: 10.1029/2018JB016558

Johnson, S. S., Mischna, M. A., Grove, T. L., & Zuber, M. T. 2008, Journal of Geophysical Research: Planetsal Research: Planets, 113, E08005, doi: 10.1029/2007JE002962

Katz, R. F., Spiegelman, M., & Langmuir, C. H. 2003, Geochemistry, Geophysics, Geosystems, 4, 1073, doi: 10.1029/2002GC000433

Kawamoto, T., & Holloway, J. R. 1997, Science, 276, 240, doi: 10.1126/science.276.5310.240

Kelemen, P. B., & Manning, C. E. 2015, Proceedings of the National Academy of Sciences, 112, E3997, doi: 10.1073/pnas.1507889112

Kelemen, P. B., Matter, J., Streit, E. E., et al. 2011, Annual Review of Earth and Planetary Sciences, 39, 545, doi: 10.1146/annurev-earth-092010-152509

Kelley, D. S., Karson, J. A., Fruh-Green, G. L., et al. 2005, Science, 307, 1428

Klein, F., Grozeva, N. G., & Seewald, J. S. 2019, Proceedings of the National Academy of Sciences, 116, 17666, doi: 10.1073/pnas.1907871116

Korenaga, J. 2003, Geophysical Research Letters, 30, 1437, doi: 10.1029/2003GL016982

—. 2006, in Archean Geodynamics and Environments, ed. K. Benn, J.-C. Mareschal, & K. Condie (AGU, Washington, D.C.), 7–32, doi: 10.1029/164GM03

—. 2007, Journal of Geophysical Research, 112, B05408, doi: 10.1029/2006JB004502

—. 2010, Journal of Geophysical Research, 115, B11405, doi: 10.1029/2010JB007670

—. 2011, Journal of Geophysical Research, 116, B12403, doi: 10.1029/2011JB008410

—. 2017, Earth and Planetary Science Letters, 457, 1, doi: 10.1016/j.epsl.2016.10.011

—. 2020, Earth-Science Reviews, 205, 103185, doi: 10.1016/j.earscirev.2020.103185

Korenaga, J., Planavsky, N. J., & Evans, D. A. D. 2017, Philosophical Transactions of the Royal Society A, 375, 20150393, doi: 10.1098/rsta.2015.0393

Krissansen-Totton, J., Arney, G. N., & Catling, D. C. 2018, Proceedings of the National Academy of Sciences, 115, 4105, doi: 10.1073/pnas.1721296115

Lambert, J. B., Gurusamy-Thangavelu, S. A., & Ma, K. 2010, Science, 327, 984, doi: 10.1126/science.1182669

Lebrun, T., Massol, H., Chassefière, E., et al. 2013, Journal of Geophysical Research: Planets, 118, 1155, doi: 10.1002/jgre.20068

Lyubetskaya, T., & Korenaga, J. 2007, Journal of Geophysical Research, 112, B03211, doi: 10.1029/2005JB004223

Matsui, T., & Abe, Y. 1986, Nature, 319, 303

Maurice, M., Tosi, N., Samuel, H., et al. 2017, Journal of Geophysical Research: Planets, 122, 577, doi: 10.1002/2016JE005250

Mckenzie, D. 1984, Journal of Petrology, 25, 713, doi: 10.1093/petrology/25.3.713

Miller, N. C., Lizarralde, D., Collins, J. A., Holbrook, W. S., & Van Avendonk, H. J. 2021, Journal of Geophysical Research: Solid Earth, 126, doi: 10.1029/2020JB020982

Miyazaki, Y., & Korenaga, J. 2017, The Astrophysical Journal, 849, 41, doi: 10.3847/1538-4357/aa8cd1

—. 2019, Journal of Geophysical Research: Solid Earth, 124, 3399, doi: 10.1029/2018JB016928

Nakajima, S., Hayashi, Y.-Y., & Abe, Y. 1992, Journal of the Atmospheric Sciences, 49, 2256, doi: 10.1175/1520-0469(1992)049⟨2256:ASOTGE⟩2.0.CO;2

Parsons, B. 1982, Journal of Geophysical Research, 87, 289

Pehrsson, S. J., Eglington, B. M., Evans, D. A., Huston, D., & Reddy, S. M. 2016, Geological Society Special Publication, 424, 83, doi: 10.1144/SP424.5

Peterson, M. N. A. 1966, Science, 154, 1542, doi: 10.1126/science.154.3756.1542

Plesa, A.-C., Tosi, N., & Breuer, D. 2014, Earth and Planetary Science Letters, 403, 225, doi: 10.1016/j.epsl.2014.06.034

Proskurowski, G., Lilley, M. D., Seewald, J. S., et al. 2008, Science, 319, 604, doi: 10.1126/science.1151194

Raymond, S. N., Schlichting, H. E., Hersant, F., & Selsis, F. 2013, Icarus, 226, 671, doi: 10.1016/j.icarus.2013.06.019

Salvador, A., Massol, H., Davaille, A., et al. 2017, Journal of Geophysical Research: Planets, 122, 1458, doi: 10.1002/2017JE005286

Schulte, M., Blake, D., Hoehler, T., & McCollom, T. 2006, Astrobiology, 6, 364

Sleep, N. H., Meibom, A., Fridriksson, T., Coleman, R. G., & Bird, D. K. 2004, Proceedings of the National Academy of Sciences, 101, 12818, doi: 10.1073/pnas.0405289101

Sleep, N. H., & Zahnle, K. 2001, Journal of Geophysical Research, 106, 1373, doi: 10.1029/2000JE001247

Sleep, N. H., Zahnle, K., & Neuhoff, P. S. 2001, Proceedings of the National Academy of Sciences, 98, 3666, doi: 10.1073/pnas.071045698

Solomatov, V. S. 2007, in Treatise on Geophysics, Vol. 9 (Elsevier B.V.), 91–119

Syracuse, E. M., van Keken, P. E., & Abers, G. A. 2010, Physics of the Earth and Planetary Interiors, 183, 73, doi: 10.1016/j.pepi.2010.02.004

Tackley, P. J. 2015, in Treatise on Geophysics, Second Edition, Vol. 7 (Elsevier B.V.), 521–585, doi: 10.1016/B978-0-444-53802-4.00134-2

Tonks, W. B., & Melosh, H. J. 1993, Journal of Geophysical Research, 98, 5319, doi: 10.1029/92JE02726

Tronnes, R. G., & Frost, D. J. 2002, Earth and Planetary Science Letters, 197, 117, doi: 10.1016/S0012-821X(02)00466-1

Wilde, S. A., Valley, J. W., Peck, W. H., & Graham, C. M. 2001, Nature, 409, 175, doi: 10.1038/35051550

Wirth, E. A., & Korenaga, J. 2012, Earth and Planetary Science Letters, 357-358, 111, doi: 10.1016/j.epsl.2012.09.010

Zahnle, K., Arndt, N., Cockell, C., et al. 2007, Space Science Reviews, 129, 35, doi: 10.1007/s11214-007-9225-z

Zahnle, K. J., Kasting, J. F., & Pollack, J. B. 1988, Icarus, 74, 62

Zahnle, K. J., Lupu, R., Dobrovolskis, A., & Sleep, N. H. 2015, Earth and Planetary Science Letters, 427, 74, doi: 10.1016/j.epsl.2015.06.058

Zhang, G., Mei, S., & Song, M. 2020, Geophysical Research Letters, 47, e2019GL085895, doi: 10.1029/2019GL085895